GEOLOGICA CARPATHICA, OCTOBER 2016, 67, 5, 417–432 doi: 10.1515/geoca-2016-0026

Age and origin of fluorapatite-rich dyke from Baranec Mt. (Tatra Mts., Western Carpathians): a key to understanding of the post-orogenic processes and element mobility

ALEKSANDRA GAWĘDA[1] ✉, KRZYSZTOF SZOPA[1], DAVID CHEW[2], URS KLÖTZLI[3], AXEL MÜLLER[4], MAGDALENA SIKORSKA[5], PAULINA PYKA[1]

[1]Faculty of Earth Sciences, University of Silesia ul. Będzińska 60, 41-200 Sosnowiec, Poland; ✉aleksandra.gaweda@us.edu.pl
[2]Department of Lithospheric Research, University of Vienna, Althanstrasse 14, 1090 Vienna, Austria
[3]Department of Geology, School of Natural Sciences, Trinity College Dublin, Dublin 2, Ireland
[4]Natural History Museum, University of Oslo, P.O. Box 1172, Blindern, 0318 Oslo, Norway
[5]Polish Geological Institute-Polish Research Institute, ul. Rakowiecka 4, Warsaw, Poland

(Manuscript received January 10, 2016; accepted in revised form September 22, 2016)

Abstract: On the southeastern slope of the Baranec Mount in the Western Tatra Mountains (Slovakia) an apatite-rich pegmatite-like segregation was found in the subvertical fault zone cutting metapelitic rocks. Two zones: felsic (F) and mafic (M) were found, differing in mineral assemblages and consequently in chemistry. Fluorapatite crystals yield a LA-ICP-MS U-Pb age of 328.6±2.4 Ma. A temperature decrease from 634 °C to 454 °C at a pressure around 500 to 400 MPa with oxygen fugacity increasing during crystallization are the possible conditions for formation of the pegmatite-like segregation, while secondary alterations took place in the temperature range of 340–320 °C. The Sr-Nd isotope composition of both apatite and whole rock point toward a crustal origin of the dike in question, suggesting partial melting of (P, F, H_2O)-rich metasedimentary rocks during prolonged decompression of the Tatra Massif. The original partial melt (felsic component) was mixed with an external (F, H_2O)-rich fluid, carrying Fe and Mg fluxed from more mafic metapelites and crystallizing as biotite and epidote in the mafic component of the dyke.

Key words: dyke, apatite, U-Pb apatite age, Tatra Mountains.

Introduction

Syntectonic veins cutting metamorphic complexes are important in deciphering the geological processes acting during uplift and decompression in collisional orogens (Druguet et al. 2008; Chen et al. 2012). Such veins, being a result of channelized fluid/melt flow, are discordant or parallel to host rock foliation and could be classified as pegmatites (Liebscher et al. 2007; Chen et al. 2012). In particular, the mineral assemblages and geochemical features of pegmatite-like mineral segregations carry information about the partial melting processes, the origin and evolution of the melts and fluids during plate subduction, new melt generation and the interaction between fluid, melt and country rocks during decompression (e.g., Miller et al. 2002; Schmidt & Poli 2003; Lü et al. 2012). The mineral composition of such veins is simple (feldspar, quartz, micas, amphiboles, pyroxenes, epidote-group minerals in different proportions, with accessories like garnet, zircon and apatite; Chen et al. 2012; Lü et al. 2012) and they do not show the typical pegmatite zonation (Simmons & Webber 2008).

Fluorapatite-rich veins are rarely found in the Tatra Mountains (Fig. 1a,b) and were subdivided as a special type, differing from the typical muscovite-type pegmatites (Gawęda 1993, 1995). The muscovite-type pegmatites were connected to a muscovite dehydration melting process, and dated by whole-rock Rb-Sr method at ca. 345 Ma (Gawęda 1995). On the southeastern slope of the Baranec Mount (Western Tatra Mountains; Fig. 1b,c) an apatite-rich pegmatite-like dyke was found in a subvertical fault zone, which also hosts an eclogite boudin and is bordered by strongly mylonitized metapelitic rocks (Fig. 1c). The aim of this paper is to decipher the origin and age of the apatite-rich pegmatite-like dyke. Apatite LA-ICP-MS U-Pb dating was used to constrain the timing of crystallization and decompression activity which is then compared to published data from the crystalline basement of the Tatra Mountains.

Geological setting and sample description

The Tatra Mountains represent the northernmost crystalline core of several "core mountains", present within the realm of the Central Western Carpathians (Fig. 1a,b). The crystalline core of the Tatra Mountains comprises a Variscan polygenetic granitoid pluton and its metamorphic envelope (Fig. 1b; Morozewicz 1914; Kohút & Janák 1994; Gawęda et al. 2016). Crystalline rocks are partly covered by Mesozoic sedimentary successions as a result of the Alpine orogenesis. The metamorphic envelope to the polygenetic granitoid intrusion is exposed mostly in the western part of the massif and is strongly migmatized at 365–360 Ma (Burda & Gawęda

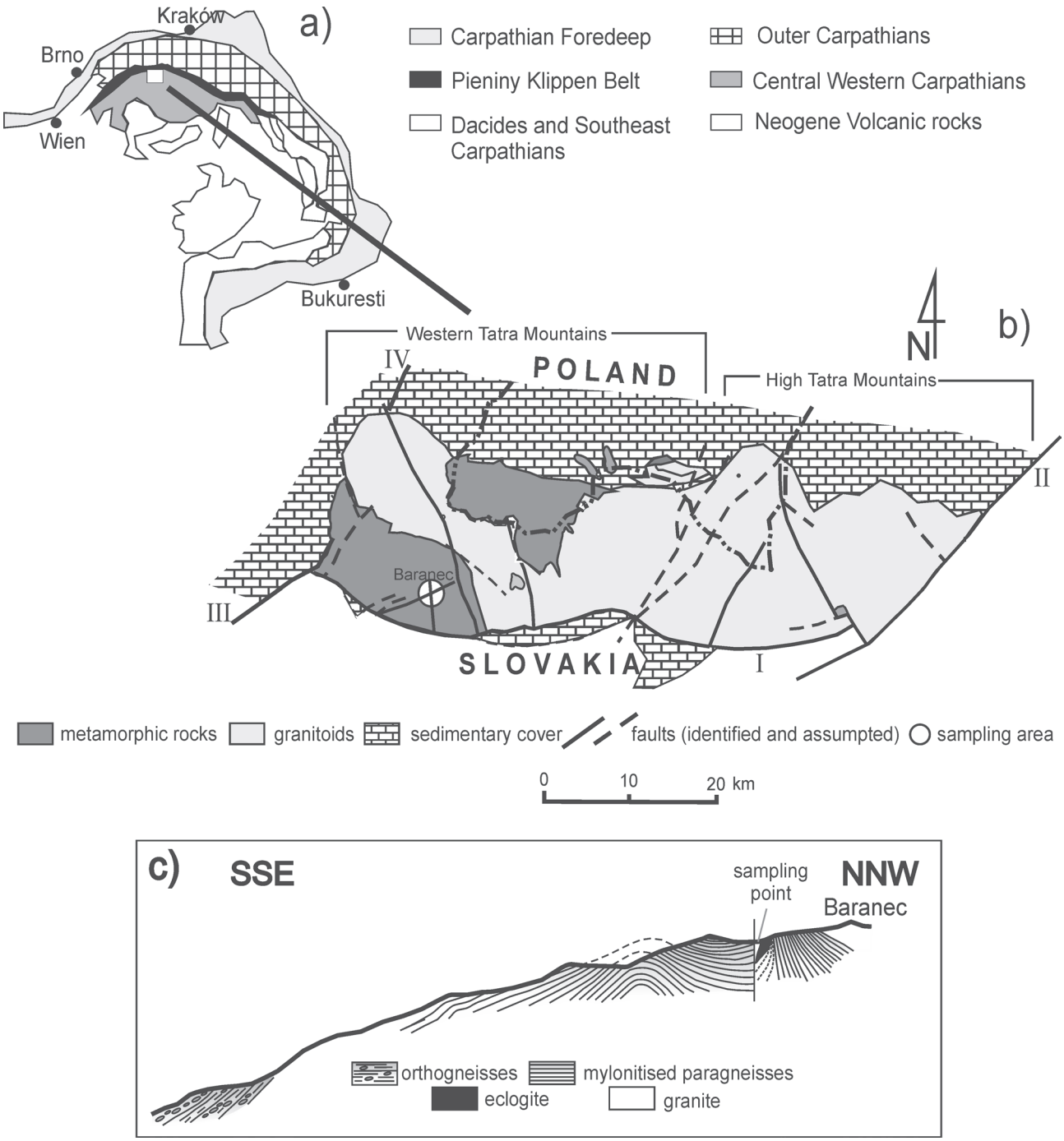

Fig. 1. Simplified geological sketch of the Carpathians (a), schematic geological map of the Tatra Mountains (according to with the location sampling area (b) with cross-section through the Baranec Mt. (c).

2009; Fig. 1b). The tabular granitoid pluton is composed of several magma batches, with U–Pb zircon emplacement ages between 370 and 340 Ma (Poller & Todt 2000; Poller et al. 2000; Kohút et al. 2010; Burda et al. 2011, 2013a,b; Kohút & Siman 2011; Gawęda et al. 2016).

The amphibolite facies envelope rocks are cut by dykes and lenses of anatectic pegmatites. These show a classical zonation, with an aplitic zone, a graphic zone, a blocky feldspar zone and a quartz core (Gawęda 1993, 1995). The mineralogy of the pegmatite is simple: quartz, K-feldspar, albite, muscovite, occasionally schorl-dravite tourmaline (Gawęda et al. 2002). The pegmatites belong to the muscovite class of Černý & Ercit (2005). A whole-rock Rb-Sr age of 345±9 Ma (Gawęda 1995) is consistent with K-Ar dating of muscovite megacrysts, at 343±9 Ma (Deditius 2004), and is temporally associated with the youngest magmatic activity in the Tatra Mountains, dated by the U-Pb method by zircon at 350–340 Ma, with maximum peak at

345 Ma (Gawęda 2008; Burda et al. 2013a; Gawęda et al. 2016). Variscan exhumation of the Tatra crystalline massif, post-dating the intrusion, was suggested to have occurred at ca. 340 Ma, with cooling rate of ca. 30 °C/Ma (Moussalam et al. 2012). Recent LA-ICP-MS U-Pb dating of fluorapatite crystals from Tatra granitoids has demonstrated that the end of high temperature tectomagmatic activity in the crystalline rocks of the Tatra Mountains took place at ca. 340 Ma (Gawęda et al. 2014).

The investigated coarse-grained dyke was found on the southeastern slope of Baranec Mount (Western Tatra Mountains) within the sub-vertical fault zone (Fig. 1c). The vein is bordered by mylonitic gneisses to the south and by an eclogite boudine to the north, and its maximum thickness in outcrop is ~1 metre. The dyke contains two components: "mafic" (M) and "felsic" (F), up to 10–20 cm in size, chaotically distributed within the vein (Fig. 2a,b). The northern margin, close to the eclogite boudin, is enriched in the mafic components. The felsic component is composed of plagioclase (locally antiperthitic) up to 2 cm in size and quartz, sporadically showing graphic-like intergrowths, euhedral prismatic fluorapatite crystals up to 15 mm long (Fig. 2b,c), and REE-rich epidote as an accessory component. The mafic parts consist of dark mica (up to 1 cm in diameter), short prismatic fluorapatite (Fig. 2b,d), plagioclase, quartz and allanite-(Ce) to epidote as main minerals, and accessory K-feldspars, muscovite and Mn-rich ilmenite. The very coarse grained (cm-size) texture and local presence of plagioclase-quartz graphic intergrowths in "F"-component resemble the pegmatite, but a typical pegmatite zonation is lacking, which calls into question the classification position of the analysed segregation.

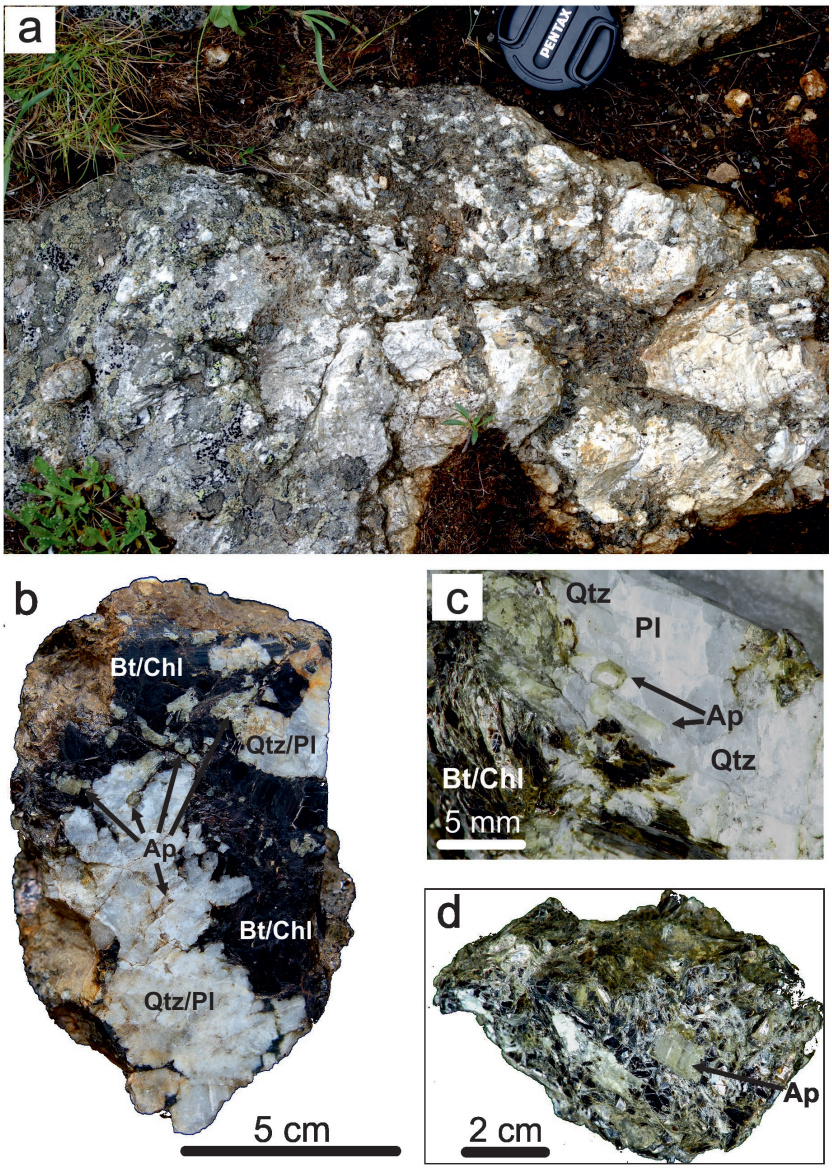

Fig. 2. Textures of the pegmatite-like dyke from the Baranec Mount: **a** — photograph showing occurrence of the pegmatite-like vein and its "patchy" internal texture; **b** — details of the "patchy" texture of the vein showing the relations of mafic to felsic components; **c** — ball-shaped and short-prismatic apatite crystals in felsic component; **d** — prismatic apatite crystals in mafic component.

Sampling and experimentals

Sampling, microscopy and whole rock analyses

Three samples were selected for analyses: one representing the felsic component ("F"), the second representing the mafic ("M") component and the third, in the amount of ~5 kg, representing a mixture of both types ("T"), in equal proportions ("F+M"). The microscopic observations were carried out at the Faculty of Earth Sciences, University of Silesia, using an Olympus BX-51 microscope. The whole rock analyses of three samples (F, M, T) were done by XRF for major and LILE trace elements and ICP-MS for HFSE and REE in the ACME Analytical Laboratories (Canada). REE were normalized to C1 chondrite (Sun & McDonough 1989).

Electron probe micro analyses (EPMA)

Microprobe analyses of main and accessory minerals were done in the Inter-Institutional Laboratory of Microanalyses of Minerals and Synthetic Substances, Warsaw, using

a Cameca SX 100 electron microprobe operating in the wavelength-dispersive spectroscopic (WDS) mode under the following conditions: 15 kV accelerating voltage, 20 nA beam current, 1–5 μm beam diameter, peak count-time of 20 s and background time of 10 s. Standards, analytical lines, diffracting crystals and mean lower detection limits (in wt. %) were as follows: barite — S (Kα, PET, 0.04), apatite — P (Kα, PET, 0.03), diopside — Mg (Kα, TAP, 0.02), orthoclase — Al (Kα, TAP, 0.02), Si — (Kα, TAP, 0.02) and K (Kα, PET, 0.03), GaAs — As (Mα, PET, 0.04), ThO_2 — Th (Mα, PET, 0.04), wollastonite — Ca (Kα, PET, 0.03), $Y_3Al_5O_{12}$ — Y (Lα, TAP, 0.04), La-rich glass — La (Lα, PET, 0.03), CeP_5O_{14} — Ce (Lα, PET, 0.03), $NdGaO_3$ — Nd (Lβ, LIF, 0.03), $STiO_3$ — Sr (Lα, TAP, 0.03) hematite — Fe (Ka, LIF, 0.09), rhodohrosite — Mn (Kβ, LIF, 0.03), scapolite — Cl (Kα, PET, 0.03), phlogopite — F (Kα, TAP, 0.04). The apatite analyses have been normalized to the sum of 50 negative charges including 24 oxygen ions and two monovalent anions (fluorine site), according to the ideal chemical formula of fluorapatite: $A_{10}(BO_4)_6(X)_2$ where site A is occupied by Ca, Fe, Mn, Mg, Th, REE, Y and Na, site B by P (substituted by S, Si) and site X by F, Cl and OH group. For all others minerals, their normalization parameters as well as limits of detection (LoD) are given in tables.

Cathodoluminescence

CL images of feldspars were obtained using CCL 8200 mk3 apparatus (Cambridge Image Technology Ltd.), mounted on an Optiphot 2 Nikon microscope in Polish Geological Institute — National Research Institute, Warsaw. The applied acceleration voltage was 20 kV, the beam current 500 mA and the vacuum 67–27 Pa.

Isotopic analyses

The Sm-Nd and Rb-Sr analytical work was performed at the Laboratory of Geochronology, Department of Lithospheric Research, University of Vienna. Results are based on ID-TIMS procedure.

Sample digestion for Nd-Sr analysis was performed in Savillex® beakers using an ultrapure 4:1 mixture of HF and HNO_3 for 10 days at 110 °C on a hot plate. For whole rock powders, a minimum dissolution time of 3 weeks was applied to ensure complete leaching of the REEs from refractory material. After evaporating the acids, repeated treatment of the residue using HNO_3 and 6 N HCl resulted in clear solutions for all samples. The REE fraction was extracted using AG® 50W-X8 (200–400 mesh, Bio-Rad) resin and 4.0 N HCl. Neodymium was separated from the REE fraction using teflon-coated HdEHP, and 0.24 N HCl as elution media. Strontium separation followed conventional techniques, using AG® 50W-X8 (200–400 mesh, Bio-Rad) resin and 2.5 N HCl as eluants. Maximum total procedural blanks were <1 ng for Sr and 50 pg for Nd and were taken as negligible. Neodymium and strontium were run as metals from a Re double filament, using a ThermoFinnigan® Triton TIMS, using La Jolla (Nd) and the NBS987 (Sr) international standards, respectively. Within-run mass fractionation for Nd and Sr isotope compositions (IC) was corrected for relative to $^{146}Nd/^{144}Nd = 0.7219$, and $^{86}Sr/^{88}Sr = 0.1194$, respectively. Uncertainties on the Nd and Sr isotope ratios are quoted as $2\sigma_m$.

Laser-ablation inductively coupled plasma mass spectrometry (LA-ICP-MS) of quartz

Trace-element contents in quartz were determined using laser ablation inductively coupled plasma mass spectrometer (LA-ICP-MS) at the Geological Survey of Norway, Trondheim. It is a double focusing sector field instrument (ELEMENT-1 Finnigan MAT) combined with a New Wave UP-193 nm excimer laser probe. Continuous raster ablation was carried out, resulting in ablated rasters of approximately 150×100 nm with depths of 20 to 30 μm. Element concentrations were calculated by multi-standard calibration. Limits of detection (LoD) are listed in table of data. The analytical error ranges within 10 % of the absolute concentration of the element. Detailed description of the measurement procedures were given by Flem et al. (2002) and Flem & Müller (2012).

Fluorapatite analyses and dating

Apatite crystals separated by handpicking were mounted in 25 mm diameter epoxy resin pucks, then ground and polished to expose the grain interiors. The fluorapatite crystal morphologies were imaged by scanning electron microscopy on a FET Philips 30 electron microscope (15 kV and 1 nA) at the Faculty of Earth Sciences, University of Silesia, Sosnowiec, Poland.

For trace element and isotopic analyses apatite crystals were selected from mafic and felsic components. Apatite U-Pb data were acquired using a Photon Machines Analyte Exite 193 nm ArF Excimer laser-ablation system coupled to a Thermo Scientific iCAP Qc at the Department of Geology Trinity College Dublin. Twenty eight isotopes (^{31}P, ^{35}Cl, ^{43}Ca, ^{55}Mn, ^{86}Sr, ^{89}Y, ^{139}La, ^{140}Ce, ^{141}Pr, ^{146}Nd, ^{147}Sm, ^{153}Eu, ^{157}Gd, ^{159}Tb, ^{163}Dy, ^{165}Ho, ^{166}Er, ^{169}Tm, ^{172}Yb, ^{175}Lu, ^{200}Hg, ^{204}Pb, ^{206}Pb, ^{207}Pb, ^{208}Pb, ^{232}Th, ^{238}U and mass $^{248}(^{232}Th^{16}O)$ were acquired using a 50 μm laser spot, a 4 Hz laser repetition rate and a fluence of 3.31 J/cm^2. A Madagascar apatite (473.5±0.7 Ma; Cochrane et al. 2014) was used as the primary apatite reference material in this study while McClure Mountain syenite apatite (523.5±2.1 Ma; Chew & Donelick 2012) was used as a secondary standard. NIST 612 standard glass was used as the apatite trace element concentration reference material. The raw isotope data were reduced using the "VizualAge" data reduction scheme (Petrus & Kamber 2012) of the freeware IOLITE package of Paton et al. (2011). Sample-standard bracketing was applied after the correction of down-hole fractionation to account for long-term drift in isotopic or elemental ratios by normalizing all ratios to those

of the U-Pb reference standards. Common Pb in the primary apatite standard was corrected using the ^{207}Pb-based correction method using a modified version of the VizualAge DRS (Chew et al. 2014). Over the course of two months of analyses, the McClure Mountain apatite secondary standard (^{207}Pb/^{235}U TIMS age of 523.51±1.47 Ma; Schoene & Bowring 2006) yielded a U-Pb Tera-Wasserburg Concordia lower intercept age of 524.5±3.7 Ma with an MSWD=0.72. The regression line was anchored to a lower intercept using a ^{207}Pb/^{206}Pb value of 0.88198, derived from an apatite ID-TIMS total U-Pb isochron (Schoene & Bowring 2006). REE contents were normalized to C1 chondrite (Sun & McDonough 1989).

Results

Petrography and mineral chemistry

Plagioclase crystals in the felsic component of the vein are andesine ($An_{30}Ab_{70}$–$An_{35}Ab_{65}$), they show typical mechanical twinning (so-called ladder structures; Fig. 3a) and a greenish CL colour (Fig. 3b). Locally they reveal antiperthitic exsolutions of K-feldspar with a composition of $Or_{93\text{-}95}$ (Table 1). Plagioclase in the mafic component has an oligoclase composition ($An_{22}Ab_{75}Or_2$–$An_{27}Ab_{70}Or_3$). Small K-feldspar crystals straddle the contact between apatite and plagioclase crystals (Fig. 4a) and coexist with REE-rich epidote and muscovite (Fig. 4b). Formation of secondary tiny epidote needles, showing bright yellow-green CL colours (Fig. 3c; Table 2), is a product of alteration (albitization) of plagioclase. Mean value of ^{207}Pb/^{206}Pb ratio from 6 plagioclase crystals equals 0.8611±0.0051.

Quartz in the felsic component is intergrown with plagioclase while in the mafic component milky to smoky quartz fills the wedge-shaped intracrystalline fractures in plagioclases. The trace elements content in quartz differs slightly between the two components (Table 3). Aluminium, the most common trace elements in quartz (e.g., Götze et al. 2001; Müller et al. 2003), is low in both zones, with similar concentrations compared to published Al concentrations in magmatic and hydrothermal quartz elsewhere (e.g., Jourdan et al. 2009; Müller et al. 2010), while Li is very low, even when compared to low-Li post-magmatic quartz from the High Tatra Mts. (Gawęda et al. 2013). Titanium content is higher in quartz in the mafic component (26.6–34.7 ppm) in relation of quartz in the felsic component (23.4–28.3 ppm; Table 3).

Pale-green fluorapatite crystals are present in both components and exhibit different morphologies: from ball-shaped to prismatic ones (Fig. 2c,d), but no important differences in chemistry were noted. They are all fluorapatite (Table 4), rich in REE (total REE content=2009–4940 ppm). Yttrium contents range from 750 ppm to 1468 ppm, while Sr range from 261 to 638 ppm. High Mn contents (1220–2496 ppm) cause the typical yellow CL emission (Table 5; Fig. 3d). The chondrite-normalized REE diagram exhibits a minor LREE enrichment (Ce_N/Yb_N=5.19–8.17), together with the presence of a pronounced negative Eu anomaly (Eu/Eu*=0.24–0.29) and a slight positive Ce anomaly (Ce/Ce*=1.09–1.12; Fig. 5; Table 5). The moderately negative slope of the LREE patterns (La_N/Sm_N=0.3–0.6) and strongly fractionated HREE patterns (Gd_N/Lu_N=11.7–13.0) are relatively consistent throughout the analysed grains (Table 5, Fig. 5). The ^{87}Sr/^{86}Sr ratio in apatite is high and equal to 0.719175, with an age-corrected ^{143}Nd/^{144}Nd ratio of 0.511699 (Table 6).

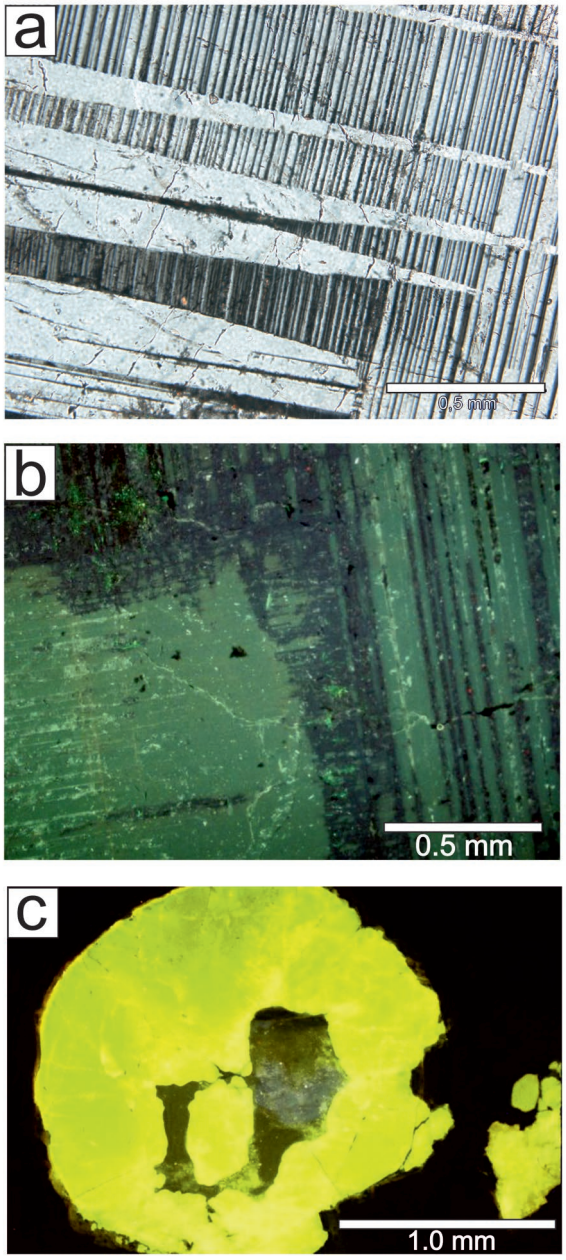

Fig. 3. Microphotographs and cathodoluminescence (CL) images showing textural aspects of the apatite-rich pegmatite-like dike from Baranec Mt. **a** — ladder structures in plagioclase, crossed polars; **b** — CL image of plagioclase with characteristic yellowish-greenish colour; **c** — apatite crystal with characteristic bright yellow CL.

Dark mica flakes up to 10 mm in diameter and brick-red–pale-yellow pleochroic scheme show ferroan phlogopite composition, with Fe/(Fe+Mg)=0.47–0.50 and Ti in the range of 0.29–0.35 [*a.p.f.u.*] (Table 7). The flakes are ductile deformed, without visible cracks. The phlogopite chloritization is restricted, and is associated with formation of secondary titanite and epidote. Chlorite is represented by clinochlore–chamosite, according to the Nomenclature Committee of the AIPEA (Bailey 1988). The Fe/(Fe+Mg) ratio attains 0.5–0.72 (Table 8). However, the chlorite composition shows a relatively wide range of $Al^{IV}/(Al^{IV}+Si)$ ratios, ranging from 0.26 to 0.40. Rare muscovite crystals are zoned in respect to Mg and Si distribution, decreasing from the core to the rim, while Na increases in the opposite way (Table 6).

Minerals of the epidote group show the strong but irregular zonation with respect to REE (Figs. 3b,c; 6), they belong to allanite-(Ce) and epidote, with ΣREE_{oxide}=25.0–0.6 wt. %, Ce enriched relative to La and U enriched relative to Th (Table 2). Primary ilmenite (Table 9) forms tiny inclusions in dark mica, shows titanite coronas (Fig. 4d). These secondary titanite crystals are moderately enriched in F, Al and Fe (Table 10).

Table 1: Feldspar composition and temperature estimated using Fuhrman and Lindsley (1988) two-feldspar geothermometry fluorapatite-rich dyke from Baraniec Mt., Tatra Mts.

Feldspar composition	Ab	Or	An
plagioclase original/adjusted	0.756/0.709	0.048/0.028	0.239/0.263
alkali feldspar original/adjusted	0.045/0.084	0.933/0.916	0.022/0.000
Concordant temperature [°C]	495	495	495
Average temperature [°C]	495		
plagioclase original/adjusted	0.658/0.638	0.000/0.020	0.342/0.342
alkali feldspar original/adjusted	0.124/0.116	0.845/0.879	0.031/0.005
Concordant temperature [°C]	549	549	549
Average temperature [°C]	549		

Fluorapatite dating

LA-ICP-MS U-Pb fluorapatite data points are aligned along a discordia as a result of variable incorporation of

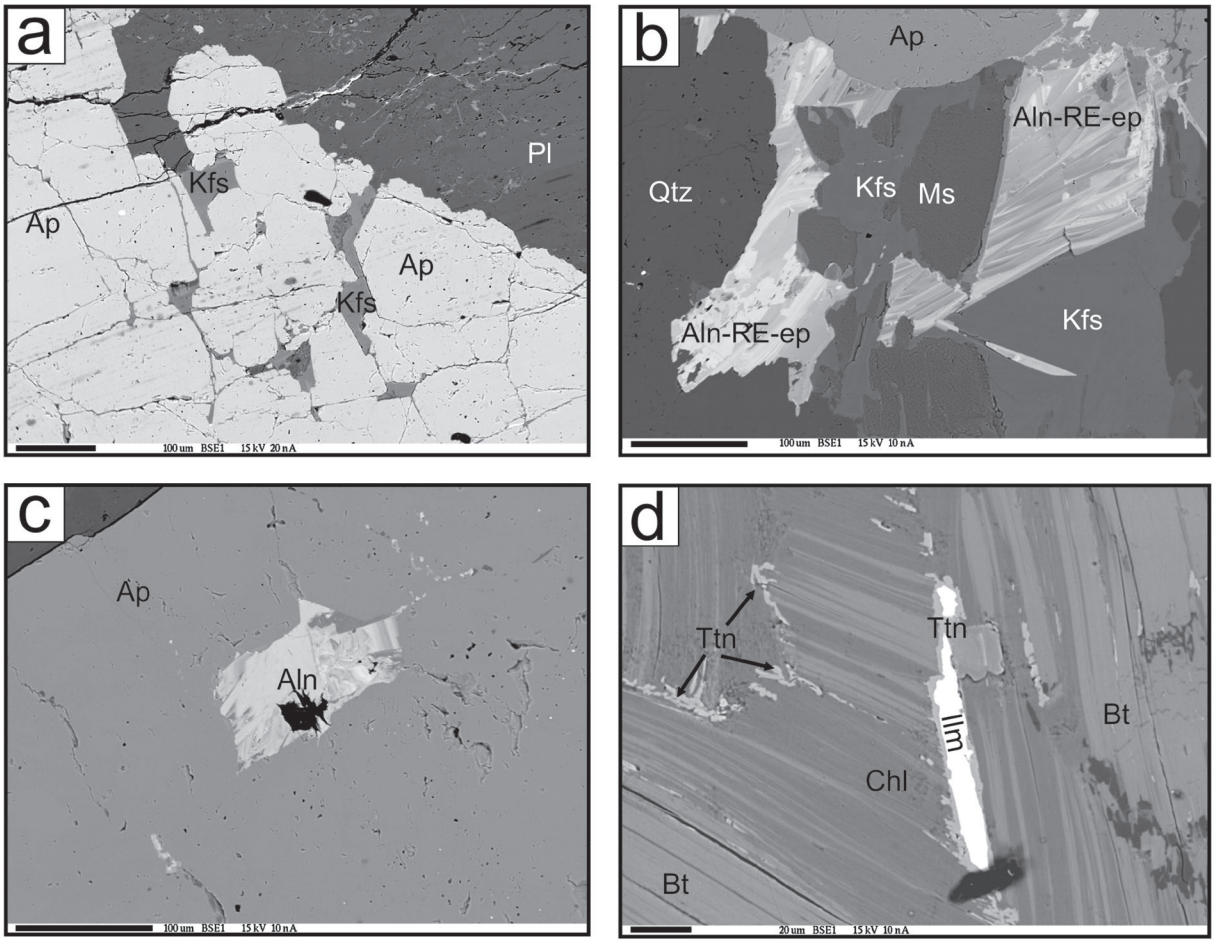

Fig. 4. BSE images of minerals from apatite-rich pegmatite-like dike. **a** — irregular growth contact of plagioclase (Pl) and apatite (Ap), with K-feldspar (Kfs) crystallizing at the border; **b** — allanite-epidote (Aln-REep) overgrowing the apatite (Ap) and filling the interstices between K-feldspar (Kfs), muscovite (Ms) and quartz (Qtz); **c** — allanite (Aln) inclusion in apatite (Ap); **d** — secondary titanite (Ttn) associated with biotite (Bt) chloritization and overgrowing ilmenite (Ilm).

Table 2: Selected analyses of allanite-(Ce) and epidote with their crystal-chemical formulae (according to Armbruster et al. 2006).

Compound (wt. %)	LoD	Allanite-(Ce)				Epidote	
		#1	#2	#3	#4	#5	#6
SiO_2	0.05	30.96	31.56	32.41	33.17	36.75	37.92
TiO_2	0.03	0.04	0.16	b.d.l.	0.18	0.03	0.03
UO_2	0.13	0.13	0.23	0.18	b.d.l.	b.d.l.	b.d.l.
Al_2O_3	0.01	18.14	18.67	20.74	19.70	23.81	26.37
Y_2O_3	0.05	0.27	0.62	2.31	1.05	0.15	0.05
La_2O_3	0.08	3.34	2.96	2.54	2.39	0.16	0.08
Ce_2O_3	0.01	9.60	8.56	6.79	6.49	0.37	0.10
Pr_2O_3	0.01	1.69	1.20	1.34	1.11	0.06	0.10
Nd_2O_3	0.29	6.68	6.07	4.56	3.86	b.d.l.	0.29
Sm_2O_3	0.01	1.68	1.58	0.87	0.87	0.00	0.00
Gd_2O_3	0.33	1.10	0.76	1.21	0.60	b.d.l.	b.d.l.
Fe_2O_3	0.07	1.23	1.94	1.10	4.81	12.03	9.36
FeO	----	10.87	9.82	7.94	6.72	0.09	0.10
MnO	0.05	1.57	1.84	0.52	0.52	0.02	0.03
MgO	0.01	0.17	0.14	0.48	0.14	0.11	0.01
CaO	0.03	9.32	10.47	12.87	14.92	22.58	23.46
F	0.15	0.23	0.16	b.d.l.	b.d.l.	b.d.l.	b.d.l.
H_2O calc.		1.50	1.56	1.63	1.65	1.86	1.89
Total		99.72	99.43	98.38	98.93	98.05	99.80
Crystal-chemical formulae calculated to 8 cations							
Si^{4+}		2.992	2.994	2.989	2.998	2.979	2.988
Ti^{4+}		0.003	0.011	–	0.012	0.002	0.002
U^{4+}		0.001	0.005	0.002	–	–	–
Al^{3+}		2.066	2.087	2.254	2.099	2.275	2.448
Y^{3+}		0.014	0.031	0.113	0.050	0.006	0.002
La^{3+}		0.119	0.104	0.086	0.080	0.005	0.002
Ce^{3+}		0.340	0.297	0.229	0.215	0.011	0.003
Pr^{3+}		0.060	0.041	0.045	0.037	–	–
Nd^{3+}		0.231	0.206	0.150	0.125	0.002	0.003
Sm^{3+}		0.056	0.052	0.028	0.027	–	–
Gd^{3+}		0.035	0.024	0.037	0.018	–	–
Fe^{3+}		0.089	0.139	0.077	0.327	0.734	0.555
Mn^{2+}		0.120	0.147	0.041	0.040	0.001	0.002
Mg^{2+}		0.024	0.020	0.066	0.018	0.013	0.001
Fe^{2+}		0.878	0.779	0.613	0.508	0.006	0.007
Ca^{2+}		0.965	1.064	1.271	1.445	1.961	1.980
∑ REE		0.840	0.723	0.576	0.501	0.023	0.014

Note: All iron has been measured as Fe^{+3}; b.d.l. — below detection limit. LoD — limit of detection.

common Pb. The apatite sample yields a Tera-Wasserburg lower intercept age of 328.6±2.4 Ma (MSDW=0.75; Table 11; Fig. 7). The discordia was anchored using the Stacey & Kramers (1975) terrestial Pb evolution model calculated for the apatite U–Pb age. The corresponding unanchored lower intercept age is 334±14 Ma.

Whole rock chemistry of fluorapatite-rich vein

The felsic component shows high SiO_2 (72.1 wt. %), Al_2O_3 (16.0 wt. %), Na_2O (4.7 wt. %.) and CaO (3.8 wt. %) concentrations, while in the mafic component high P_2O_5 (10.5 wt. %) and total Fe as Fe_2O_3 (9.8 wt. %) contents are characteristic (Table 12). Among trace elements Y and V show the highest contents in the mafic component. Rare earth element (REE) concentrations also differ in both vein components (Fig. 5;

Table 3: Trace elements content of quartz from fluorapatite-rich dyke and calculated crystallization temperatures.

Sample/ Element	LoD	*"F"*			*"M"*		
		#1	#2	#3	#1	#2	#3
Li	0.07	2.20	2.36	1.54	1.33	1.80	1.33
B	1.04	2.93	2.09	2.61	4.91	3.07	5.41
Mn	0.11	0.39	0.53	0.46	bdl	0.34	0.22
Ge	0.06	1.34	1.05	1.00	0.78	1.08	1.05
Sr	0.01	1.52	4.26	1.28	0.01	bdl	1.48
Al	6.6	43.91	38.71	40.43	44.57	31.20	46.90
P	2.5	b.d.l.	b.d.l.	b.d.l.	2.61	2.87	b.d.l.
Ti	1.5	24.86	28.34	23.36	26.64	29.55	34.68
T_{min} [°C]		594	606	589	600	609	624
T_{max}[°C]		613	625	608	620	629	645
T_{mean}[°C]		604	616	598	610	619	634

Note: All data obtained by laser ablation inductively coupled plasma mass spectrometry (LA-ICP-MS). The crystallization temperatures of quartz T_{min}, T_{max}, T_{mean} were calculated applying the Ti-in-geothermometer by Wark and Watson (2006). LoD = Limit of Detection. ***"F"***— felsic and ***"M"***— mafic.

Table 12). Chondrite (C1)-normalized REE pattern of the felsic component displays a positive Eu anomaly (Eu/Eu*= 5.45) and weak REE fractionation (Ce_N/Yb_N=4.18). The REE pattern of the mafic component characterized by a negative Eu anomaly (Eu/Eu*=0.28) and also weak REE fractionation (Ce_N/Yb_N=7.09; Fig. 5; Table 12). Isotope composition of T sample recalculated to 328 Ma is $(^{143}Nd/^{144}Nd)_{328}$= 0.511711, ε_{Nd}^{328}=–9.9 and I_{Sr}^{328}=0.72837 (Table 6). Trace element "spider" diagrams normalized to primitive mantle (PM) for all samples do not show a significant fractionation between large-ion lithophile elements (LILE) and high field strength elements (HFSE) (Fig. 8). Strongly negative Th anomalies, coexisting with U enrichment, negative Zr and Hf anomalies and slightly negative Nb anomalies are characteristic of all the samples, while Ta anomalies are lacking. Positive and negative Sr anomalies in the felsic and mafic components are observed respectively (Fig. 8), similarly to the positive and negative Eu anomalies in chondrite-normalized REE diagrams (Fig. 5), consistent with plagioclase being the main carrier of Sr and Eu.

Discussion

Emplacement mechanism and pressure-temperature-oxygen fugacity estimations

The textures observed in feldspars, like mechanical twinning and the ductile deformations of biotite flakes point out the vein intrusion was syntectonic (Brown & Parsons 1994). The cooling time for a relatively small dyke (approx. 1 m in diameter) should not be long, so one can expect the chilled margin around the contact in the case of the temperature difference, which, however, is not present. This suggests that host rocks were warm enough to prevent the chilled margin formation or metasomatic character of the vein.

Table 4: Representative electron-microprobe analyses and crystal-chemical formulae of fluorapatite.

component	LoD	1	2	3	4	5	6	7
P_2O_5	0.70	42.63	42.15	41.89	42.46	42.29	42.79	42.25
FeO	0.01	0.12	0.11	0.11	0.16	0.33	0.22	0.36
MnO	0.01	0.49	0.70	0.07	1.10	0.55	0.37	0.42
CaO	0.56	54.81	54.54	54.39	54.53	54.88	55.07	54.67
Na_2O	0.01	0.10	0.12	b.d.l.	0.09	b.d.l.	b.d.l.	b.d.l.
H_2O calc.		0.48	0.35	0.36	0.45	0.06	0.17	0.32
F	0.17	2.78	3.01	2.96	2.83	3.65	3.45	3.10
Cl	0.01	0.00	0.00	0.00	0.07	0.00	0.00	0.00
–O=F+Cl		1.17	1.27	1.25	1.21	1.54	1.45	1.31
Total		100.24	99.72	98.54	100.48	100.22	100.61	99.81
Crystal-chemical formulae calculated to 13 anions								
P^{5+}		3.015	3.004	3.013	3.005	3.000	3.016	3.005
Fe^{2+}		0.008	0.008	0.008	0.011	0.023	0.015	0.025
Mn^{2+}		0.035	0.050	0.005	0.078	0.039	0.026	0.030
Ca^{2+}		4.906	4.919	4.951	4.885	4.927	4.912	4.921
Na^{+}		0.016	0.020	0.000	0.015	–	–	–
Σ *M*		4.965	4.997	4.964	4.989	4.989	4.953	4.976
OH^{-}		0.265	0.199	0.205	0.252	0.033	0.092	0.176
F^{-}		0.735	0.801	0.795	0.748	0.967	0.908	0.824
Cl^{-}		–	–	–	0.010	–	–	–
Σ *X*		1.000	1.000	1.000	1.000	1.000	1.000	1.000

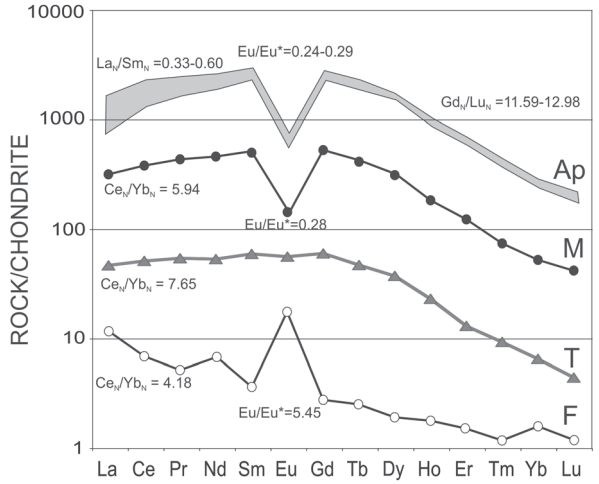

Fig. 5. Chondrite (C1)-normalized REE patterns of apatite crystals from apatite-rich pegmatite-like dyke, whole rock sample (**T**), mafic component (**M**) and felsic component (**F**).

The Ti concentrations in quartz (Table 3) have been used for calculation of the quartz crystallization temperature, applying the Ti-in-quartz geothermometer of Wark & Watson (2006). Quartz from the felsic component crystallized between 598 and 616 °C, while quartz from the mafic component exhibits crystallization temperatures 610–634 °C (Table 3), both supporting the late magmatic origin of the segregation. The presence of antiperthitic exsolution in plagioclase enables ternary feldspar temperatures to be calculated. Results for the computations yield temperatures of 495–550 °C (Table 1), interpreted as cooling conditions.

The amount of phengite substitution in the muscovite core was used to calibrate the pressure (Table 7; Massone & Schreyer 1987) which is in the range of 400–500 MPa.

The regression equations according to Kranidiotis & MacLean (1987) and Cathelineau & Nieva (1985) procedures were used to establish the temperature range of the chlorite's formation from the chemical composition of chlorites formed at the expense of biotite. The temperature calculations reveal one crystallization interval, with the average temperature at 323 °C and at 336 °C, respectively (Table 8; Fig. 9) that could be consistent with the low pressure muscovite rims (Table 7), suggesting a clockwise cooling P-T path. Late fluid circulation causing the secondary alterations in this temperature range and at very low pressure (Fig. 9) is in agreement with P-T conditions stated elsewhere in the Tatra Mountains (Gawęda & Włodyka 2012).

The enrichment in LREE and the presence of pronounced negative Eu anomalies in the chondrite-normalized REE patterns of fluorapatite (Fig. 5), the relatively high Ti content of biotite (Table 7) and the presence of primary ilmenite (Fig. 4d), indicate oxidizing conditions in an early crystallization stage of the mafic component. The presence of minerals from the epidote group both as inclusions in apatite (Fig. 3c) and as the late mineral, overgrowing fluorapatite (Fig. 4b), suggest more oxidizing conditions. The presence of the secondary titanite coronas on ilmenite (Fig. 4d) also associated with biotite chloritization marks the late, low temperature oxidation event (Harlow et al. 2006; Fig. 9). The positive Eu anomaly in the felsic component of a dyke is likely a result of the abundance of plagioclase which is a carrier of Eu^{2+}, suggesting rather reduced conditions in felsic component of the pegmatite-like segregation. All these facts could be a result of local oxygen fugacity fluctuations during crystallization.

Timing of the vein intrusion and its relation to the granite

Taking into account the relatively low closure temperature of the U-Pb system in fluorapatite (375–550 °C; Chamberlain & Bowring 2000; Schoene & Bowring 2007; Cochrane et al. 2014), and the crystallization temperatures obtained in this study, the apatite U-Pb age of 328 Ma could be interpreted as the time of the cooling of the dyke. The apatite U-Pb system records subsequent cooling of the granitoid intrusion at 340 Ma (Gawęda et al. 2014), and these rocks seem unlikely to be the source of apatite-rich melt. Fluorapatite-rich rocks are present in the Tatra Mountains (Gawęda 2008; Szopa et al. 2013), however they are commonly associated with the oldest magmatic episode at ca. 368 Ma (Burda et al. 2011; Szopa et al. 2013) and show U-Pb apatite cooling age of ~340 Ma (Gawęda et al. 2014). Multi-stage boron-rich fluids, also enriched in phosphorus and fluorine, have been

Table 5: Representative LA-ICP-MS analyses of Mn, Sr, Y, REE contents in apatite crystals with selected petrological indicators.

Sample	Element (ppm)																	Calculated indicators				
	Mn	Sr	Y	La	Ce	Pr	Nd	Sm	Eu	Gd	Tb	Dy	Ho	Er	Tm	Yb	Lu	Eu/Eu*	Ce/Ce*	La_N/Sm_N	Ce_N/Yb_N	Gd_N/Lu_N
R1_1	2330.0	589.1	1411.0	377.4	1270.0	203.1	1088.0	397.9	42.22	506.4	76.25	382.6	52.01	97.5	9.48	41.86	4.82	0.29	1.10	0.59	8.17	12.99
R1_2	2119.0	538.4	1381.0	311.4	1108.0	181.8	995.0	373.2	36.94	481.9	73.15	370.5	50.78	97.0	9.29	41.36	4.61	0.26	1.12	0.52	7.22	12.92
R1_3	2271.0	568.9	1437.0	351.7	1220.0	197.3	1061.0	392.5	39.52	491.7	76.34	385.7	53.59	102.0	9.81	44.20	4.9	0.27	1.11	0.56	7.44	12.40
R1_4	2496.0	637.7	1555.0	413.7	1378.0	218.4	1176.0	434.4	46.20	545.6	83.10	416.8	56.88	108.0	10.49	47.16	5.28	0.29	1.10	0.60	7.87	12.77
R1_5	2363.0	539.5	1416.0	355.6	1217.0	195.5	1045.0	382.4	36.91	481.1	74.54	377.4	53.07	101.0	9.76	43.15	4.95	0.26	1.11	0.58	7.60	12.01
R1_6	2433.0	557.9	1440.0	370.9	1241.0	198.8	1060.0	389.3	38.10	492.2	76.30	389.3	53.81	102.7	9.75	44.39	5.16	0.26	1.10	0.60	7.53	11.79
R1_7	2437.0	547.8	1396.0	363.0	1215.0	198.5	1049.0	375.6	37.37	479.1	73.84	375.7	52.55	100.9	9.72	43.77	4.93	0.27	1.09	0.61	7.48	12.01
R1_8	1291.0	261.2	749.7	107.6	469.2	86.9	508.6	202.1	18.12	256.5	40.01	205.2	28.74	54.05	5.28	24.24	2.603	0.24	1.16	0.33	5.21	12.18
R1_9	2181.0	513.2	1353.0	333.9	1157.0	187.7	1017.0	367.9	35.47	468.6	72.40	369.9	51.48	98.0	9.44	42.73	4.77	0.26	1.11	0.57	7.29	12.14
R1_10	1967.0	490.8	1343.0	290.9	1059.0	176.3	973.0	360.9	33.72	460.8	71.47	364.8	51.18	98.0	9.48	42.02	4.74	0.25	1.12	0.51	6.79	12.02
R1_11	2234.0	526.3	1383.0	336.0	1158.0	188.1	1022.0	371.0	36.67	471.1	73.22	373.1	51.80	99.4	9.59	43.18	4.88	0.27	1.10	0.57	7.22	11.93
R1_12	2156.0	511.8	1360.0	319.7	1121.0	183.8	1001.0	368.3	34.53	466.7	71.95	367.8	51.45	98.2	9.56	42.88	4.87	0.25	1.11	0.54	7.04	11.84
R1_13	2329.0	550.7	1406.0	358.7	1216.0	196.4	1035.0	380.9	38.13	482.5	74.31	377.2	52.46	100.6	9.51	43.68	4.97	0.27	1.10	0.59	7.50	12.00
R1_14	2267.0	532.2	1394.0	338.2	1161.0	188.4	1023.0	373.8	36.41	472.3	73.43	372.9	52.31	99.8	9.50	43.45	4.96	0.26	1.10	0.57	7.20	11.77
R1_15	2293.0	539.2	1410.0	351.1	1207.0	194.4	1037.0	379.4	37.18	482.0	74.34	381.0	52.52	100.9	9.64	43.53	4.96	0.26	1.11	0.58	7.47	12.01
R1_16	2287.0	544.5	1422.0	353.5	1212.0	196.3	1050.0	384.7	38.00	485.2	74.90	382.9	52.72	100.8	9.73	43.69	4.94	0.27	1.10	0.58	7.47	12.14
R1_17	2360.0	568.8	1414.0	350.7	1204.0	194.6	1047.0	380.6	39.75	487.3	74.90	382.8	53.02	101.8	9.73	43.35	4.9	0.28	1.10	0.58	7.48	12.29
R1_18	2431.0	599.3	1443.0	376.7	1264.0	204.4	1086.0	392.5	42.48	495.2	76.70	392.3	54.52	103.3	9.81	44.36	4.88	0.29	1.09	0.60	7.68	12.54
R1_19	2413.0	593.1	1418.0	372.9	1253.0	201.0	1065.0	387.3	41.44	488.1	75.20	387.5	53.99	101.4	9.74	43.73	4.86	0.29	1.10	0.60	7.72	12.41
R1_20	2015.0	546.4	1448.0	330.2	1186.0	197.7	1053.0	383.3	37.87	488.5	75.66	388.7	54.13	103.3	9.63	44.58	4.92	0.27	1.11	0.54	7.17	12.27
R1_21	2104.0	537.1	1410.0	322.4	1125.0	185.0	1002.0	371.8	36.36	471.4	73.29	379.7	52.61	99.9	9.56	43.47	4.883	0.26	1.10	0.54	6.97	11.93
R1_22	21550	554.4	1468.0	340.9	1173.0	192.7	1037.0	386.8	37.57	484.0	76.46	390.2	54.61	104.3	10.15	44.75	5.16	0.26	1.10	0.55	7.06	11.59
R1_23	1351.0	481.4	1382.0	186.8	817.0	149.8	876.0	348.2	32.37	457.3	72.00	371.1	52.00	99.1	9.49	42.41	4.73	0.25	1.17	0.34	5.19	11.95
R1_24	1822.0	495.7	1441.0	281.5	1040.0	178.8	978.0	371.6	34.41	479.7	74.67	386.4	53.62	102.7	9.80	44.35	5.06	0.25	1.11	0.47	6.32	11.72
R1_25	1894.0	522.8	1423.0	291.4	1062.0	178.0	984.0	370.4	34.91	475.2	74.60	380.2	53.24	101.8	9.64	43.82	4.96	0.25	1.12	0.49	6.53	11.84
R1_26	1220.0	488.3	1387.0	205.6	865.3.0	156.8	899.7	357.5	32.9	463.4	72.83	375.9	51.88	100.3	9.42	42.87	4.76	0.25	1.16	0.36	5.44	12.03
LoD	0.04	2.85	0.01	0.01	0.01	0.00	0.01	0.01	0.01	0.01	0.01	0.01	0.01	0.01	0.00	0.01	0.00					

Table 6: Rb-Sr and Sm-Nd analyses of the whole-rock (**TWR**) and fluorapatite separated grains (**ap**).

Lp	Sample No	Rb [ppm]	Sr [ppm]	$^{87}Rb/^{86}Sr$	$^{87}Sr/^{86}Sr$	±	I_{Sr}^{328}	Sm [ppm]	Nd [ppm]	$^{147}Sm/^{144}Nd$	$^{143}Nd/^{144}Nd$	±	ε_{Nd}^{328}	T_{DM} (Ga)
1.	T_{WR}	34.1	363.6	0.267826	0.728370		0.727120	72.63	200.76	0.28680	0.512181	0.000005	–9.85	1.82
2.	Ap	–	532.17	–	0.719175		0.719175	372.47	1006.47	0.223713	0.512179	0.000004	–10.086	1.83

Compound (wt. %)	LoD	Ferroan phlogophite						Muscovite		
		#1	#2	#3	#4	#5	#6	core	mantle	rim
SiO_2	0.01	36.01	36.17	36.18	36.25	35.71	36.29	47.91	46.5	46.67
TiO_2	0.02	2.83	2.96	2.97	3.04	2.88	3.05	b.d.l.	0.17	0.22
Al_2O_3	0.01	17.60	17.46	17.62	17.79	18.09	17.45	33.53	33.16	36.18
Cr_2O_3	0.03	b.d.l.	b.d.l.	0.03	0.05	0.06	b.d.l.	b.d.l.	0.03	b.d.l.
FeO	0.02	17.82	18.04	17.96	18.07	17.89	18.23	0.49	1.99	1.33
MnO	0.03	0.24	0.22	0.33	0.23	0.24	0.25	0.02	b.d.l.	b.d.l.
MgO	0.02	10.87	10.77	10.85	11.00	11.25	10.50	2.01	1.71	0.80
BaO	0.02	0.13	0.46	b.d.l.	b.d.l.	0.11	b.d.l.	0.55	0.15	0.28
Na_2O	0.02	0.07	b.d.l.	0.10	0.21	0.09	0.04	0.22	0.25	1.21
K_2O	0.02	9.44	9.60	9.52	9.23	8.87	9.60	11.13	11.09	9.41
H_2O calc.		3.99	4.01	4.02	4.04	4.00	4.01	4.53	4.46	4.56
Total		99.00	99.71	99.56	99.89	99.19	99.42	100.4	99.5	100.66
Crystal-chemical formulae calculated on the basis of 22 O^{2-}										
Si^{4+}		5.467	5.466	5.462	5.447	5.398	5.489	6.345	6.258	6.140
Ti^{4+}		0.323	0.336	0.338	0.344	0.327	0.347	–	0.017	0.022
$^{IV}Al^{3+}$		2.533	2.59	2.6	2.61	2.65	2.57	1.65	1.74	1.86
$^{VI}Al^{3+}$		0.617	0.49	0.51	0.5	0.54	0.51	3.58	3.52	3.75
Cr^{2+}		–	–	0.001	0.002	0.007	–	–	0.001	–
Fe^{2+}		2.263	2.280	2.268	2.271	2.262	2.306	0.055	0.224	0.146
Mn^{2+}		0.031	0.028	0.042	0.029	0.031	0.032	0.003	–	–
Mg^{2+}		2.461	2.426	2.443	2.464	2.536	2.367	0.396	0.343	0.158
Ba^{2+}		0.007	0.027	–	–	0.007	–	0.029	0.008	0.015
Na^{+}		0.022	0.006	0.029	0.061	0.027	0.010	0.057	0.064	0.309
K^{+}		1.828	1.851	1.833	1.769	1.710	1.853	1.880	1.905	1.580
#fm		0.482	0.488	0.486	0.483	0.475	0.497	0.122	0.395	0.480

Note: #fm=Fe/(Fe+Mg+Mn). b.d.l. — below detection limit

Table 8: Representative analyses of chlorite-group minerals and their crystal-chemical formulae and with Fe^{2+}/Fe^{3+} and OH calculated assuming full site occupancy. Computed temperatures of crystallization are according to Kranidiotis & MacLean (1987) and Cathelineau & Nieva (1985) procedures.

Compound (wt.%)	LoD	Sample									
		#1	#2	#3	#4	#5	#6	#7	#8	#9	#10
SiO_2	0.03	26.65	25.77	26.11	26.54	25.76	25.95	26.22	34.71	35.13	35.22
TiO_2	0.05	0.05	0.08	0.14	0.06	0.07	0.06	0.07	3.14	3.12	3.23
Al_2O_3	0.04	18.61	19.74	19.18	15.94	19.66	19.86	19.91	16.76	16.45	16.99
FeO	0.15	27.23	27.03	27.36	37.88	29.36	28.20	28.51	22.30	21.60	21.78
MnO	0.14	0.23	0.22	0.32	0.22	0.49	0.49	0.42	0.42	0.38	0.33
MgO	0.04	15.05	13.91	14.40	8.35	11.68	12.20	12.74	8.29	8.39	8.28
CaO	0.06	0.06	b.d.l.	b.d.l.	b.d.l.	b.d.l.	b.d.l.	b.d.l.	b.d.l.	b.d.l.	b.d.l.
Na_2O	0.04	b.d.l.	b.d.l.	b.d.l.	b.d.l.	b.d.l.	b.d.l.	0.04	0.08	0.07	0.05
K_2O	0.05	b.d.l.	0.06	b.d.l.	b.d.l.	b.d.l.	0.06	b.d.l.	2.06	2.01	1.25
H_2O calc.		11.11	12.97	11.44	9.95	11.04	11.09	11.22	11.75	12.21	11.34
Total		99.03	99.84	99.08	98.96	98.16	98.03	99.17	99.57	99.36	98.53
Crystal-chemical formulae calculated on the basis of 28 O^{2-}											
Si^{4+}		5.664	5.538	5.580	5.912	5.747	5.599	5.592	6.883	6.973	6.958
$^{VI}Al^{3+}$		2.336	2.462	2.420	2.088	2.253	2.401	2.408	1.117	1.027	1.042
$^{IV}Al^{3+}$		2.326	2.545	2.414	2.098	2.262	2.666	2.609	2.935	2.956	3.049
Ti^{4+}		0.008	0.013	0.023	0.010	0.012	0.010	0.011	0.468	0.466	0.480
Fe^{3+}		0.003	0.053	0.022	0.017	0.019	0.154	0.116	1.299	1.366	1.515
Fe^{2+}		4.837	4.805	4.869	7.040	5.602	4.935	4.969	2.400	2.219	2.083
Mn^{2+}		0.041	0.040	0.058	0.042	0.095	0.090	0.076	0.071	0.064	0.055
Mg^{2+}		4.768	4.456	4.588	2.773	3.986	3.924	4.050	2.451	2.482	2.438
Ca^{2+}		0.014	–	–	–	–	–	–	–	–	–
Na^{+}		–	–	–	–	–	–	0.033	0.062	0.054	0.038
K^{+}		–	0.033	–	–	–	0.033	–	1.042	1.018	0.630
OH^{-}		16.000	16.000	16.000	16.000	16.000	16.000	16.000	16.000	16.000	16.000
Σ Cations		36.00	35.95	35.99	35.98	35.83	35.83	35.87	34.10	34.03	34.01
Fe/(Fe+Mg)		0.50	0.52	0.52	0.72	0.59	0.56	0.56	0.60	0.59	0.60
T_1 (°C)		314	335	328	275	336	348	348	344	352	353
T_2 (°C)		303	318	313	293	317	324	325	326	331	332

Notes: b.d.l. – below detection limit. LoD – limit of detection.

Table 7: Micro-chemical analyses of micas from fluorapatite-rich dyke and their crystal-chemical formulae.

documented within the Tatra Massif and are associated with hydrofracturing, boron metasomatism and molybdenite crystallization, but are dated at 350±1 Ma (Gawęda et al. 2013), which is roughly 22 Ma older than the pegmatite dated in this study and hence should be excluded as the direct source of P and F. The chondrite-normalized REE patterns of apatite differ slightly from those of Tatra granitoids, showing higher REE fractionation indices (Table 5; Fig. 5; cf.: Gawęda et al. 2016).

The U-Pb apatite age, determined in this study fits well with the ^{40}Ar-^{39}Ar age range (330–300 Ma) obtained for micas from the High Tatra granite (Kohút and Sherlock 2003). The U-Th-Pb ages of secondary monazite-(Ce) crystals from the Western Tatra Mountains, also cluster at ~330 Ma (Burda & Dzierżanowski 2005) and they are in agreement (within age uncertainties) of the U-Pb fluorapatite age of 328.6±2.4 Ma.

Origin of the parent melt/fluid to the fluorapatite-rich vein

The analysed vein is unzoned and does not show any typical pegmatite internal structure (e.g. Simmons & Webber 2008; London 2009). The chemical composition of both mafic and felsic components are also not conclusive. The major element composition of the felsic component is governed by the abundant plagioclase and quartz, while mafic component chemistry is a result of fluorapatite and ferroan phlogopite concentrations. Among trace elements, V show increased concentration

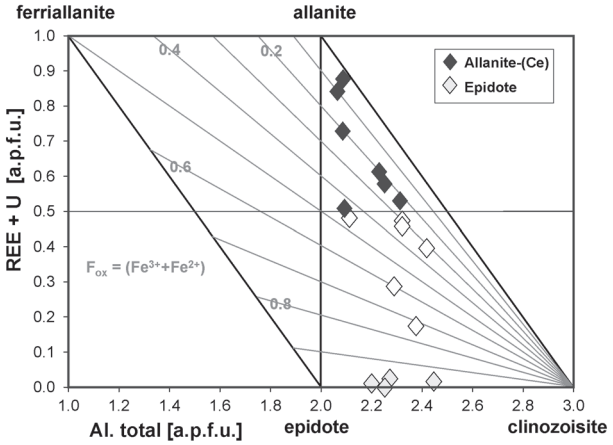

Fig. 6. Projection of the epidote-group minerals composition on the (REE+U) versus Al [a.p.f.u.] (after Petrík et al. 1995).

Table 9: Representative analyses and crystal-chemical formulae of ilmenite.

Component (wt. %)	LoD	#1	#2	#3
TiO_2	0.03	51.04	51.47	49.99
Cr_2O_3	0.03	0.03	b.d.l.	b.d.l.
Fe_2O_3	0.07	2.10	1.22	3.26
FeO	0.07	39.14	39.56	38.44
MnO	0.07	6.52	6.52	6.26
MgO	0.02	0.09	0.07	0.09
Total		98.95	98.89	98.04
Crystal-chemical formulae based on 6 O^{2-}				
Ti^{4+}		1.954	1.972	1.929
Cr^{2+}		0.001	–	–
Fe^{3+}		0.080	0.047	0.126
Fe^{2+}		1.667	1.685	1.650
Mn^{2+}		0.281	0.281	0.272
Mg^{2+}		0.007	0.006	0.007
∑ Cations		3.990	3.991	3.984

Notes: b.d.l. — below detection limit. LoD — limit of detection.

in titanite, while fluorapatite is a main Y carrier, both phases showing enrichment in the pegmatite mafic component. Chondrite-normalized REE-patterns of the felsic component, with positive Eu anomaly, are typical of feldspar-governed fractions, while negative Eu anomaly in mafic component mirrors the geochemical characteristics of apatite and the minerals of the epidote group. In the primitive mantle-normalized multi-element diagrams (Sun & McDonough, 1989) negative Nb and positive Ta anomalies are present, suggesting atypical arc setting (Thirwall et al. 1994) but another process (fractional crystallization?) overlapping the source characteristics. Trace element characteristics of the felsic component (Sr/Y=86.63; Table 12) suggest slab melting and its adakitic *sensu lato* provenance (Moyen 2009), while mafic component trace element chemistry shows no such relationships (Table 12). Isotopic signatures also point out no mantle/lower crustal influence, which is necessary to characterize the adakitic melts, even those not connected to slab melting (Macpherson et al. 2006).

Table 10: Representative analyses and crystal-chemical formulae of titanite.

Compound (wt. %)	LoD	#1	#2
SiO_2	0.01	30.66	28.73
TiO_2	0.03	36.19	39.5
Al_2O_3	0.01	2.52	0.92
V_2O_3	0.07	0.48	0.33
Cr_2O_3	0.04	0.04	b.d.l.
Fe_2O_3	0.07	1.11	1.97
MnO	0.07	b.d.l.	0.29
MgO	0.02	0.07	0.05
CaO	0.02	28.48	27.12
F	0.35	0.61	b.d.l.
O=F		0.28	–
Total		100.17	98.99
Crystal-chemical formulae based on 3 cations			
Si^{4+}		1.000	0.964
Ti^{4+}		0.893	0.995
Al^{3+}		0.101	0.039
V^{3+}		0.009	0.007
Cr^{3+}		0.001	–
Fe^{3+}		0.035	0.057
Mn^{2+}		–	0.009
Mg^{2+}		0.005	0.004
Ca^{2+}		0.991	0.973

Note: b.d.l. — below detection limit. LoD — limit of detection.

As apatite is a Rb-free phase, its Sr composition could be treated as the direct marker of its origin. The high $^{87}Sr/^{86}Sr$ ratio of apatite (0.719175) and age corrected $^{87}Sr/^{86}Sr$ ratio of the whole rock of 0.72837 suggest its crustal origin. The Sm-Nd isotopic composition of the whole-rock vein sample and fluorapatite are in agreement with the Sr data, also suggesting the crustal origin of the melt parent to the vein. Stable fluorapatite REE chemistry (Fig. 5) suggests only one melt source. The ε_{Nd}^{328} for apatite-rich segregation (–9.85; Table 6) is in the same range as for typical Tatra metapelite (ε_{Nd}^{340} = –11.32; Gawęda 2009; recalculated value ε_{Nd}^{328}=–11.13; Table 6) and from analogous metasedimentary rocks (Kohút et al., 2008). The mean $^{207}Pb/^{206}Pb$ ratio of feldspars shows a typically crustal value, supporting the former suggestions. Possibly dehydration-partial melting of the upper crust was the source of the melt parent for the dyke in question and the genetic link to the eclogite boudin could be excluded, as that shows typical mantle values (ε_{Nd}^{360}=5.0–6.7; Burda et al. 2015).

However, the computed crystallization temperatures (598–634 °C) are too low to explain the mafic component presence, which needs much higher temperatures to crystallize. Low solubility of Fe and Mg in granitic (sensu lato) melts (Puziewicz & Johannes 1988) implies these elements should be introduced to pegmatitic systems by aqueous fluids, circulating throughout the variegated country rocks and causing the mass transfer from wall rocks (Roda et al. 2004 and references therein).

The main problem is to define the rocks, which were the source for the mafic components. As Rb-Sr and Sm-Nd isotope systems are very sensitive to cation leaching and are

Table 11: Representative LA-ICP-MS U-Pb apatite data for fluorapatite-rich dyke from Baranec Mt., Slovakia.

Sample	$^{207}Pb/^{235}U$	±2σ	$^{206}Pb/^{238}U$	±2σ	ρ	$^{238}U/^{206}Pb$	±2σ	$^{207}Pb/^{206}Pb$	±2σ	ρ	$^{206}Pb/^{238}U$ age	±2σ Ma	$^{207}Pb/^{235}U$ age	±2 σ Ma	$^{207}Pb/^{206}Pb$ age	±2σ Ma	^{207}Pb corr. age	±2σ Ma	Pb_{tot} (ppm)	Th_{tot} (ppm)	U_{tot} (ppm)
R1_1	8.39	0.13	0.1194	0.0012	0.0022	20.6	0.154317	0.5069	0.0078	0.0078	727.2	6.7	2274	14	2780	250	128.56	16.9	97.88	3.25	96.85
R1_2	10.83	0.27	0.1384	0.0019	0.0029	20.8	0.151400	0.5660	0.0120	0.0120	835.0	11.0	2505	23	3400	300	121.75	36.8	96.31	2.22	75.50
R1_3	9.46	0.14	0.1292	0.0012	0.0023	23.8	0.137785	0.5322	0.0081	0.0081	783.2	6.8	2383	14	2870	280	137.20	28.0	95.48	2.67	84.65
R1_4	9.31	0.13	0.1270	0.0010	0.0022	20.2	0.136400	0.5261	0.0077	0.0077	770.7	5.9	2367	13	2850	270	109.74	27.4	130.18	4.27	118.90
R1_5	12.27	0.18	0.1514	0.0014	0.0027	22.4	0.117791	0.5846	0.0090	0.0090	908.8	8.0	2627	13	2950	310	160.50	28.8	97.54	2.58	68.75
R1_6	12.8	0.28	0.1564	0.0030	0.0038	9.0	0.155350	0.5908	0.0083	0.0083	936.0	17.0	2670	20	3190	250	131.05	30.2	100.80	3.51	70.60
R1_7	11.43	0.17	0.1474	0.0015	0.0027	23.0	0.124271	0.5682	0.0091	0.0091	886.4	8.4	2558	14	2940	290	111.96	28.5	100.25	3.07	73.90
R1_8	13.48	0.27	0.1630	0.0021	0.0033	0.0	0.124205	0.6000	0.0140	0.0140	973.0	12.0	2717	18	3610	330	107.89	35.3	54.18	0.33	34.36
R1_9	10.45	0.17	0.1363	0.0013	0.0025	21.2	0.134570	0.5539	0.0087	0.0087	824.2	7.3	2473	15	3170	250	149.51	29.6	91.61	1.81	74.41
R1_10	9.99	0.18	0.1342	0.0015	0.0026	18.6	0.144367	0.5369	0.0085	0.0085	811.8	8.6	2441	17	2900	240	110.74	17.9	86.69	1.69	73.07
R1_11	8.90	0.12	0.1240	0.0012	0.0023	20.6	0.149584	0.5192	0.0082	0.0082	753.7	6.9	2327	13	2980	220	155.60	34.8	94.08	2.79	87.21
R1_12	10.27	0.15	0.1374	0.0017	0.0027	17.9	0.143018	0.5453	0.0086	0.0086	829.9	9.7	2458	14	3040	220	94.07	36.9	93.65	2.35	77.51
R1_13	7.44	0.11	0.1128	0.0010	0.0020	20.5	0.157185	0.4782	0.0070	0.0070	688.7	6.0	2163	13	3020	240	43.07	35.1	105.21	3.88	115.20
R1_14	8.16	0.14	0.1186	0.0010	0.0021	20.2	0.149297	0.5017	0.0088	0.0088	722.3	5.8	2252	16	3010	230	55.74	32.4	94.99	2.87	95.32
R1_15	7.53	0.13	0.1123	0.0011	0.0020	19.3	0.158588	0.4852	0.0078	0.0078	686.3	6.1	2176	15	2740	280	105.11	34.7	99.35	3.34	108.00
R1_16	7.70	0.12	0.1150	0.0010	0.0020	21.3	0.151150	0.4858	0.0076	0.0076	701.8	5.7	2201	14	3000	200	106.49	30.9	98.37	3.51	104.00
R1_17	11.43	0.23	0.1468	0.0022	0.0031	20.3	0.143850	0.5680	0.0100	0.0100	882.0	12.0	2557	19	3250	260	107.75	17.1	100.77	1.89	74.25
R1_18	9.62	0.18	0.1301	0.0017	0.0026	22.1	0.153610	0.5334	0.0083	0.0083	788.5	9.9	2400	17	3150	220	141.25	33.2	104.66	2.92	93.20
R1_19	9.79	0.14	0.1306	0.0014	0.0025	19.9	0.146573	0.5425	0.0075	0.0075	791.3	8.2	2413	13	3180	250	129.32	31.1	96.61	2.61	84.50
R1_20	10.57	0.18	0.1372	0.0015	0.0026	22.2	0.138123	0.5597	0.0081	0.0081	829.0	8.5	2486	16	3120	220	65.52	42.1	85.87	1.07	67.76
R1_21	11.31	0.16	0.1443	0.0013	0.0026	20.1	0.124865	0.5651	0.0093	0.0093	868.9	7.1	2550	13	3280	190	114.25	12.0	89.78	2.57	68.30
R1_22	11.01	0.17	0.1403	0.0015	0.0026	25.8	0.132086	0.5633	0.0092	0.0092	846.2	8.3	2526	15	2980	350	124.89	13.8	96.85	2.97	75.90
R1_23	8.90	0.21	0.1177	0.0017	0.0025	18.1	0.180463	0.5490	0.0150	0.0150	718.3	9.8	2324	21	3090	300	105.06	13.0	61.00	0.61	55.99
R1_24	11.63	0.22	0.1467	0.0018	0.0029	32.0	0.134753	0.5667	0.0089	0.0089	883.3	9.8	2571	18	3220	210	122.82	13.6	83.59	2.51	62.70
R1_25	11.7	0.22	0.1497	0.0014	0.0027	21.6	0.120481	0.5670	0.0110	0.0110	898.9	8.1	2581	18	2910	270	127.76	16.3	90.32	1.51	65.30
R1_26	8.14	0.18	0.1178	0.0015	0.0024	21.4	0.172950	0.4980	0.0110	0.0110	717.8	8.8	2242	21	3060	210	119.11	13.9	62.29	1.36	63.07

usually mirrored in pegmatites showing mass transfer from mantle-related country-rocks (compare: Gawęda 1995), the eclogite, showing mantle characteristics could be excluded as the source for all "mafic" cations. The observations of the sheared metasedimentary rocks revealed, that in all of them the replacement of biotite by muscovite occur with pronounced loss of Fe and Mg (Pyka et al. 2014). Taking into account the crustal signatures of the pegmatite-like segregation, proved by the Rb-Sr, Sm-Nd and Pb isotopic systems (Table 6), the cation leaching from sheared metapelites, originally rich in Fe, Mg, Ca, is the only explanation as the source of the "mafic" cations. Liberation of P, Ca, Fe, REE and Y was possible due to monazite/xenotime decomposition by CO_2-F-H_2O–rich fluids, while Th was trapped in $ThSiO_4$ phase (Szopa 2009; Ondrejka et al. 2012). The $ThSiO_4$ phase is a common remnant in pseudomorphs after monazite-(Ce) from crystalline rocks of the Western Tatra Mountains (Szopa 2009) that explains a negative Th anomaly in primitive mantle-normalized multi-element diagrams (Fig. 8) and enrichment in P and F in the melt.

The source of fluorine is still unknown, but the circulation of F-rich fluids was noted in supra-subduction zones, due to phengite and/or F-amphibole breakdown (Sheng et al. 2013). The high activity of fluorine and phosphorus was noted during hydrothermal alterations elsewhere in the crystalline cores of the Central Western Carpathians (Burda & Dzierżanowski 2005; Szopa 2009; Uher et al 2009; Gawęda & Włodyka 2012; Ondrejka et al. 2012).

Fluid mobility was possibly enhanced by post-collisional uplift and extension. Decompression of the crystalline rocks could generate the partial melts, showing chemistry partly inherited from the melted metapelitic rocks and from the circulating (P, F, H_2O)-rich fluid which stimulated melting. The melt temperature was too low to influence the eclogite tectonically included in the system, but restricted leaching cannot be rejected, causing the oxygen fugacity fluctuations. The accumulation of volatile-rich melts could efficiently stimulate the hydraulic opening of the fractures. Fluid super-saturated magma

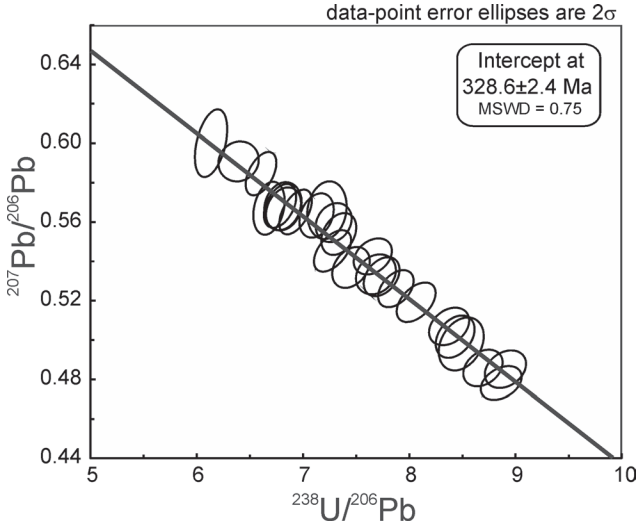

Fig. 7. Tera-Wasserburg concordia diagram anchored through common Pb for apatite from the apatite-rich pegmatite-like dike from Baranec Mt.

had been easily moved to these extensional fractures according to the magma pumping mechanism (Demartis et al. 2011). The original melt may have had the composition of the felsic component. The crystallization of abundant plagioclase causes a decrease in Ca/P ratio and limited crystallization of apatite in the felsic component (Roda et al. 2004). Phosphorus, as incompatible element (Bea et al. 1992) progressively concentrated in the late fluid, mixed with the external fluid, rich in F and H_2O, carrying the elements fluxed from more mafic metapelites, squeezed as bubbles and crystallizing the mafic component of the vein.

Although the main cooling stage is dated ~340 Ma using the same apatite U-Pb method (Gawęda et al. 2014), the younger pulses of uplift and anataxis cannot be excluded. Possibly the southern part of the Tatra metamorphic cover was affected by the multistage uplift, starting from a pre-intrusive episode, leading to the formation of kyanite-quartz segregations (Pyka et al. 2013, 2014) through syn-intrusive (Gawęda et al. 2015), late-intrusive (Gawęda et al. 2014) to post-intrusive segregation, associated with local and space-restricted magma/fluid flow.

Conclusions

1. The apatite-rich pegmatite-like dyke was emplaced syn-tectonically into a fault zone at ca. 600 °C and 400–500 MPa. Fluorapatite LA-ICP-MS U–Pb age of 328.6±2.4 Ma is interpreted as the cooling age of the dyke.

2. The Sm-Nd, Rb-Sr and $^{207}Pb/^{206}Pb$ isotope data suggest a purely crustal source for the melt/fluid parent to the pegmatite-like dyke, and no genetic link to the long-lived Variscan granitoid magmatism. A possibly source for the apatite-rich pegmatite dyke was (F, H_2O)-rich fluids, generated during exhumation of the crystalline core of the massif liberating Fe, Mg, Ca, P, REE from originally mafic metapelites, containing monazite and xenotime and which could also facilitate local partial melting.

Table 12: Chemical composition and selected petrological indicators of fluorapatite-rich dyke from Baranec Mt., Western Tatra Mountains.

Compound (wt%)	*"F"*	*"M"*	*"T"*
SiO_2	72.1	33.2	55.9
TiO_2	0.15	1.43	0.53
Al_2O_3	16.00	14.51	21.33
Cr_2O_3	0.02	0.02	0.01
$Fe_2O_3^*$	1.46	9.51	3.77
MnO	0.03	0.15	0.05
MgO	0.70	5.65	2.11
CaO	3.80	15.68	5.15
Na_2O	4.71	2.03	7.26
K_2O	0.62	4.09	0.82
P_2O_5	0.04	10.82	1.35
LOI	0.74	1.88	1.75
Total	100.37	98.95	99.98
Sr	329.2	297.6	563.60
Ba	166	590	235
Rb	25.9	224.00	34.10
Cs	2.3	17.6	2.4
Th	0.0	0.6	0.0
U	0.3	12.6	1.70
Ga	12.5	19.9	17.4
Ni	12.5	21.6	21.10
V	35	271	98
Zr	7.5	0.6	0.7
Hf	0.4	0.0	0.0
Y	3.8	277.1	34.2
Nb	1.9	17.7	8.3
Ta	0.4	1.6	0.7
La	2.7	69.8	10.50
Ce	4.1	217.1	30.00
Pr	0.48	38.08	4.88
Nd	3.00	198.7	23.60
Sm	0.54	70.53	8.61
Eu	0.98	7.78	3.08
Gd	0.56	99.95	11.67
Tb	0.09	14.29	1.67
Dy	0.49	73.33	9.03
Ho	0.10	9.70	1.25
Er	0.25	19.04	2.08
Tm	0.03	1.78	0.23
Yb	0.27	8.43	1.08
Lu	0.03	1.01	0.11
ASI	1.050	1.396	1.125
#mg	0.66	0.70	0.69
Rb/Sr	0.08	0.75	0.06
Sr/Y	86.63	1.07	16.48
Σ_{REE}	13.62	829.52	107.79
Eu/Eu**	5.45	0.28	0.94
Ce_N/Yb_N	4.18	7.09	7.65
Gd_N/Yb_N	1.72	9.81	8.94

Notes: $Fe_2O_3^*$ — total Fe as Fe_2O_3; LOI — lost of ignition;
ASI = $Al_2O_3/(CaO+Na_2O+K_2O-3.33\ P_2O_5)$ in molecular units;
#mg = Mg/(Mg+Fe) (in molecular units); Eu/Eu* = Eu/(√Sm·Gd).

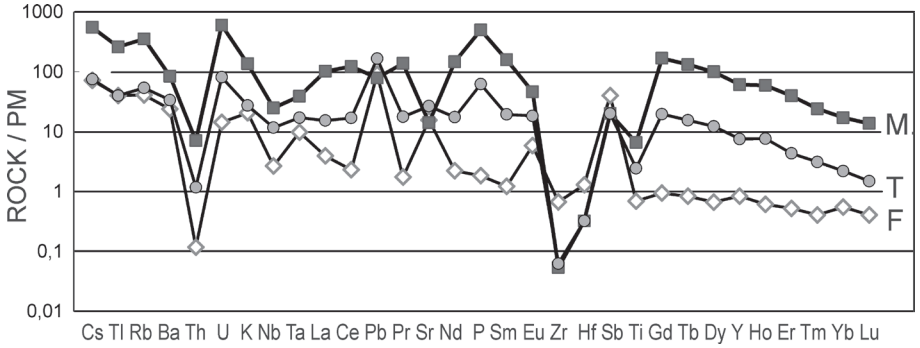

Fig. 8. Primitive mantle normalized (after Sun & McDonough 1989) trace element diagram of mafic component (M), felsic component (F) and whole-rock pegmatite-like segregation from Baranec Mt.

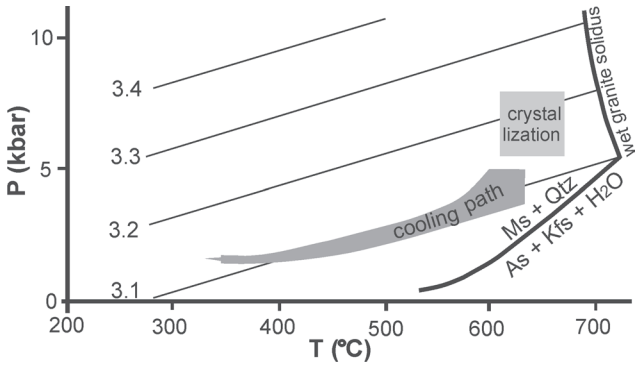

Fig. 9. Pressure (P)–temperature (T) diagram presenting the evolution of the pegmatite-like segregation.

3. The high contents of fluorine, phosphorus and water resulted in a low viscosity and high mobility of the intruding melt. Rapid crystallization with an accompanying drop in temperature and pressure resulted in disequilibrium crystallization, forming the patchy nest-like structure of the dyke and variations in oxygen fugacity during crystallization.

4. Activation of (F, H_2O, P)-rich partial melts and fluids, was possible due to post-collisional and post-magmatic uplift of the Tatra Mountains crystalline core in the supra-subduction zone.

Acknowledgements: Piotr Dzierżanowski PhD. and Mrs. Lidia Jeżak are thanked for their help during microprobe work. The extremely careful editorial corrections by Pavel Uher and reviews of Adam Pieczka and Milan Novák significantly improved the manuscript. Evgeny Galuskin is thanked for help in the mineral formula calculations. This study was financially supported by the National Science Centre (NCN) grant 2012/07/B/ST10/04366 (given to AG).

References

Armbruster T., Bonazzi P., Akasaka M., Bermanec V., Chopin C., Giere R., Heuss-Aussbichler S., Liebcher A., Manchetti S., Pan Y. & Pasero M. 2006: Recommended nomenclature of epidote-group minerals. *Eur. J. Mineral.* 18, 551–567.

Bailey S.W. 1988: Chlorites: Structures and crystal chemistry. In: Bailey S.W. (Ed.): Hydrous Phyllosilicates (Exclusive of Micas). *Reviews in Mineralogy* 19, 347–403.

Bea F., Fershater G. & Crretge L.G. 1992: The geochemistry of phosphorus in granite rocks and the effect of aluminium. *Lithos* 29, 43-56.

Brown W.L. & Parsons I. 1994: Feldspars in igneous rocks. In: Parsons I. (Ed): Feldspars and Their Reactions. NATO ASI Series, C 421, *Kluwer Academic Publishers,* Dordrecht, 449–499.

Burda J. & Dzierżanowski P. 2005: Electron microprobe dating of monazite from migmatitic gneiss from the Western Tatra Mts.: preliminary results. *Mineralogical Society of Poland – Special Papers,* 25, 277–280.

Burda J. & Gawęda A. 2009: Shear-influenced partial melting in the Western Tatra metamorphic complex: geochemistry and geochronology. *Lithos* 110, 373–385.

Burda J., Gawęda A. & Klötzli U. 2011: Magma hybridization in the Western Tatra Mountains granitoid intrusion (S-Poland, Western Carpathians). *Mineral. Petrol.* 103, 19–36.

Burda J., Gawęda A. & Klötzli U. 2013a: U-Pb zircon age of the youngest magmatic activity in the High Tatra granite. *Geochronometria* 40, 2, 134–144.

Burda J., Gawęda A. & Klötzli U. 2013b: Geochronology and petrogenesis of granitoid rocks from the Goryczkowa Unit, Tatra Mountains (Central Western Carpathians). *Geol. Carpath*. 64, 6, 419–435.

Burda J., Gawęda A., Golonka J., Majka J., Wiedenbeck M., & Pyka P. 2015: Rheic Ocean history imprinted in zircon from metabasite: a case of the Western Tatra Mountains, Poland/Slovakia. *Mineralogia – Spec. Pap*, 44, 30.

Cathelineau M. & Nieva D. 1985: A chlorite solid solution geothermometer, The Los Azufres (Mexico) geothermal system. *Contrib. Mineral. Petrol*. 91, 235–244.

Černý P. & Ercit T.S. 2005: The classification of granitic pegmatites revisited. *Can. Mineral.* 43, 2005–2026.

Chamberlain K.R. & Bowring S.A. 2000: Apatite-feldspar U-Pb thermochronometer: A reliable, mid-range (450 °C), diffusion controlled system. *Chem. Geol.* 172, 173–200.

Chen D.-L., Liu L., Sun Y., Sun W.-D., Zhu X.-H., Liu X.-M. & Guo C.-L. 2012: Felsic veins within UHP eclogite at Xitieshan in North Qaidam, NW China: partial melting during exhumation. *Lithos* 136–139, 187–200.

Chew D.M. & Donelick R.A. 2012: Combined apatite fission track and U-Pb dating by LA-ICPMS and future trends in apatite provenance analysis. In: Sylvester P. (Ed.): Quantitative Mineralogy and Microanalysis of Sediments and Sedimentary Rocks. *Mineral. Assoc. Canada*, 219–248.

Chew D.M., Petrus J.A. & Kamber B.S. 2014: U-Pb LA-ICPMS dating using accessory mineral standards with variable common Pb. *Chem. Geol.* 363, 185–199.

Cochrane R., Spikings R.A., Chew D., Wotzlaw J.-F., Chiaradia M.,

Tyrrell S., Schaltegger U. & Van der Lelijl R. 2014: High temperature (>350 °C) thermochronology and mechanisms of Pb loss in apatite. *Geochim. Cosmochim. Acta* 127, 39–56.

Deditius A. 2004: Petrology and isotopic age of the muscovite blasthesis from the mylonitic zones in the crystalline rocks of the Western Tatra Mountains). *Geologia* 16, *University of Silesia publishing House*, 133–152. (in Polish with English abstract)

Demartis M., Pinotti L.P., Coniglio J.E., D`Eramo F.J., Tubia J.M., Aragon E., Agulleiro Insula L.A. 2011: Ascent and emplacement of pegmatitic melts in a major reverse shear zone (Sierras de Cordoba, Argentina). *J. Struct. Geol.* 33, 1334–1346.

Druguet E., Czeck D.M., Carreras J. & Castaño L.M. 2008: Emplacement and deformation features of syntectonic leucocratic veins from Rainy Lake zone (Western Superior Province, Canada). *Precambrian Res.* 163, 384–400.

Flem B. & Müller A. 2012: In situ analysis of trace elements in quartz using laser ablation inductively coupled mass spectrometry. In: Götze J, Möckel R. (Eds.): Quartz deposits — Mineralogy and Analytics. *Springer Verlag*, 219–236.

Flem B., Larsen R.B., Grimstvedt A. & Masfeld J. 2002: In situ analysis of trace elements in quartz by using laser ablation inductively coupled plasma mass spectrometry. *Chem. Geol.* 182, 237–247.

Fuhrman M.L. & Lindsley D.H. 1988: Ternary-feldspar modeling and thermometry. *Am. Mineral*. 73, 201–215.

Gawęda A. 1993: Structure, mineral composition and origin of pegmatites from the Polish part of the Western Tatra Mountains. *Archiwum Mineralogiczne* 49, 2, 113–144 (in Polish with English abstract).

Gawęda A. 1995: Geochemistry and Rb/Sr isochron age of pegmatites from the Western Tatra Mts. (S-Poland). *Geol. Carpath*. 46, 95–99.

Gawęda A. 2008: Apatite-rich enclave in the High Tatra granite, Western Carpathians: petrological and geochronological study. *Geol. Carpath.* 59, 4, 295–306

Gawęda A. 2009: Enclaves in the High Tatra granite. *Univ. Silesia Publ. House, Monograph Ser*. 2637, Katowice, 1–180 (in Polish with English abstract).

Gawęda A. & Włodyka R. 2012: The origin of post-magmatic Ca-Al minerals in granite-diorite mingling zones: the Tatra granitoid intrusion, Western Carpathians. *N. Jb. Mineral. Abh*. 190, 1, 29–47.

Gawęda A., Pieczka A. & Kraczka J. 2002: Tourmalines from the Western Tatra Mountains (Central Western Carpathians): their characteristics and petrogenetic importance. *Eur. J. Mineral.* 14, 943–955.

Gawęda A., Müller A., Stein H., Kądziołko-Gaweł M. & Mikulski S. 2013: Age and origin of the tourmaline-rich hydraulic breccias in the Tatra Granite, Western Carpathians. *J. Geosci.* 58, 133–148.

Gawęda A., Szopa K. & Chew D. 2014: LA-ICP-MS U-Pb dating and REE patterns of apatite from the Tatra Mountains, Poland as a monitor of the regional tectonomagmatic activity. *Geochronometria* 41, 306–314.

Gawęda A., Szopa K. & Chew D. 2015: Variscan post-collisional cooling and uplift of the Tatra Mountains constrained by U-Pb apatite and titanite dating. *Mineralogia — Spec. Pap.* 44, 38.

Gawęda A., Burda J., Klötzli U., Golonka J. & Szopa K. 2016: Episodic construction of the Tatra granitoid intrusion (Central Western Carpathians, Poland/Slovakia): consequences for the geodynamics of Variscan collision and Rheic Ocean closure. *Int. J. Earth Sci*. 105, 1153–1174.

Götze J., Plötze M. & Habermann D. 2001: Origin, spectra characteristics and practical applications of the cathodoluminescence (CL) of quartz — a review. *Mineral. Petrol.* 71, 225–250.

Harlov D., Tropper P., Seifert W., Nijland T. & Förster H.J. 2006: Formation of Al-rich titanite ($CaTiSiO_4O$-$CaAlSiO_4OH$) reaction rims on ilmenite in metamorphic rocks as a function of fH_2O and fO_2. *Lithos* 88, 72–84.

Jourdan A.-L., Vennemann T.W., Mullis J., Ramseyer K. & Spiers C.J. 2009: Evidence of growth and sector zoning in hydrothermal quartz from Alpine veins. *Eur. J. Mineral.* 21, 219–231.

Kohút M. & Janák M. 1994: Granitoids of the Tatra Mts., Western Carpathians: Field relations and petrogenetic implications. *Geol. Carpath*. 45, 301–311.

Kohút M. & Sherlock S. 2003: Laser microprobe ^{40}Ar–^{39}Ar analysis of pseudotachylyte and host-rocks from the Tatra Mountains, Slovakia: evidence for late Palaeogene seismic/tectonic activity. *Terra Nov*a 15, 6, 417–424.

Kohút M. & Siman P. 2011: The Goryczkowa granitic type — SHRIMP dating of an original granodiorite-tonalite variety. *Mineralogia — Spec. Pap*, 38, 113–114.

Kohút M., Poller U., Gurk Ch. & Todt W. 2008: Geochemistry and U-Pb detrital zircon ages of metasedimentary rocks of the Lower Unit, Western Tatra Mountains (Slovakia). *Acta Geol. Polon.* 58, 371–384.

Kohút M., Uher P., Putiš M., Broska I., Siman P., Rodionov N. & Sergeev S. 2010: Are there any differences in age of the two principal Hercynian (I- & S-) granite types from the Western Carpathians? — A SHRIMP approach. In: Kohút M. (Ed.): Dating of minerals and rocks, metamorphic, magmatic and metallogenetic processes, as well as tectonic events. *Conferences, Symposia & Seminars, ŠGUDŠ,* Bratislava, 17–18.

Kranidiotis P. & MacLean W.H. 1987: Systematics of chlorite alteration at Phelps Dodge massive sulphide deposit, Matagami, Quebec. *Econ. Geol.* 82, 1898–1911.

Liebscher A., Franz G., Frei D. & Dulski P. 2007: High-pressure melting of eclogite and the *P–T–X* history of tonalitic to trondhjemitic zoisite-pegmatites, Münchberg Massif, Germany. *J. Petrol.* 48, 1001–1019.

London D. 2009: The origin of primary textures in granitic pegmatites. *Can. Mineral*. 47, 697–724.

Lü Z., Zhang L., Du J., Yang X., Tian Z. & Xia B. 2012: Petrology of HP metamorphic veins in coesite-bearing eclogite from western Tianshan, China: fluid processes and elemental mobility during exhumation in a cold subduction zone. *Lithos* 136–139, 168–186.

Macpherson C.G., Dreher S.T. & Thirlwall M.F. 2006: Adakites without slab melting: High pressure differentiation of island arc magma, Mindanao, the Philippines. *Earth Planet. Sci. Lett.* 243, 581–593.

Massone H.J. & Schreyer W. 1987: Phengite geobarometry based on the limited assemblage with K-feldspar, phlogopite and quartz. *Contrib. Mineral. Petrol.* 96, 212–224.

Miller J.A.**,** Buick I.S., Cartwright I. & Barnicoat A.C. 2002: Fluid processes during the exhumation of high-P metamorphic belts. *Miner. Mag.* 66**,** 93–119.

Morozewicz K. 1914: Über die Tatragranite. *N Jb Geol Paläontol Abh* 39, 289–345.

Moussallam Y., Schneider D.A., Janák M., Thoni M. & Holm D.K. 2012: Heterogeneous extrusion and exhumation of deep-crustal Variscan assembly: Geochronology of the Western Tatra Mountains, northern Slovakia. *Lithos* 144–145, 88–108.

Moyen J-F. 2009: High Sr/Y and La/Yb ratios: The meaning of the "adakitic signature". *Lithos* 112, 556-574.

Müller A., Wiedenbeck M., van der Kerkhof A.M., Kronz A. & Simon K. 2003: Trace elements in quartz — a combined electron microprobe, secondary ion mass spectrometry, laser ablation ICP-MS, and cathodoluminescence study. *Eur. J. Mineral*. 15, 747–763.

Müller A., Herrington R., Armstrong R., Seltman R., Kirwin D.J., Stenina N.G. & Kronz A. 2010: Trace elements and

cathodoluminescence of quartz in stockwork veins of Mongolian porphyry-style deposits. *Mineral. Deposita* 45, 707–727.

Ondrejka M., Uher P., Putiš M., Broska I., Bačik P., Konečny P. & Schmiedt I. 2012: Two-stage breakdown of monazite by post-magmatic and metamorphic fluids: An example of the Veporic orthogneiss, Western Carpathians, Slovakia. *Lithos* 142–143, 245–255.

Paton C., Helistrom J., Paul B., Woodhead J. & Herqt J. 2011: Iolite: freeware for the visualisation and processing of mass spectrometric data. *J. Anal. Atom. Spectrom.* 26, 2508–2518.

Petrík I., Broska I., Lipka J. & Siman P. 1995: Granitoid allanite-(Ce): substitution relations, redox conditions and REE distributions (on an example of I-type granitoids, Western Carpathians, Slovakia). *Geol. Carpath.* 46, 2, 79-94.

Petrus J.A. & Kamber B.S. 2012: VizualAge: A Novel Approach to Laser Ablation ICP-MS U-Pb Geochronology Data Reduction. *Geostandards and Geoanalytical Research* 36, 3, 247–270.

Poller U. & Todt W. 2000: U-Pb single zircon data of granitoids from the High Tatra Mountains (Slovakia): implications for the geodynamic evolution. *Transact. Royal Soc. Edinburgh: Earth. Sci*. 91, 235–243.

Poller U., Janák M., Kohút M. & Todt W. 2000: Early Variscan magmatism in the Western Carpathians: U-Pb zircon data from granitoids and orthogneisses of the Tatra Mountains (Slovakia). *Int. J. Earth Sci*. 89, 336–349.

Puziewicz J. & Johannes W. 1988: Phase equilibria and compositions of Fe-Mg-Al minerals and melts in water-saturated peraluminous granitis systems. *Contrib. Mineral. Petrol.* 100, 156–168.

Pyka P., Szopa K. & Gawęda A. 2013: Megacrysts of kyanite from Baranec Mt., Western Tatra Mountains, Slovakia. *Mineralogia* 44, 1–2, 35–41.

Pyka P., Gawęda A., Szopa K., Müller A. & Sikorska M. 2014: Petrogenesis of kyanite-quartz segregations in mica schists of the Western Tatra Mountains (Slovakia). *Mineralogia* 45, 3–4, 99–120.

Roda E., Pesquera A., Fontan F. & Keller P. 2004: Phosphate mineral association in the Cañada pegmatite (Salamance, Spain): paragenetic relatioships, chemical compositions, and implications for pegmatite evolution. *Am. Mineral.* 89, 110–125.

Schoene B. & Bowring S.A. 2006: U-Pb systematics of the McClure Mountain syenite: thermochronological constraints on the age of the Ar-40/Ar-39 standard MMhb. *Contrib. Mineral. Petrol.* 151, 5, 615–630.

Schoene B. & Bowring S.A. 2007: Determining accurate temperature-time paths from U-Pb thermochronology: An example from the Kaapval craton, southern Africa. *Geochim. Cosmochim. Acta* 71, 1, 165–185.

Sheng Y.-M., Zheng Y.-F., Li S.-N. & Hu Z. 2013: Element mobility during continental collision: insights from polymineralic metamorphic vein within UHP eclogite in the Dabie orogen. *J. Metam. Geol.* 31, 221–241.

Schmidt M.-W. & Poli S. 2003: Generation of mobile components during subduction of oceanic crust. *Treatise on Geochemistry* 3, 567–591.

Simmons Wm.B., Webber K.L. 2008: Pegmatite genesis: state of the art. *Eur. J. Mineral.* 20, 421–438.

Stacey J.S. & Kramers J.D. 1975: Approximation of terrestrial lead isotope evolution by a two stage model. *Earth Planet. Sci. Letters* 26, 207–221.

Sun S.S. & McDonough W.F. 1989: Chemical and isotopical systematics of oceanic basalts: implications for mantle composition and processes. Magmatism in the Oceanic Basins. *Geol. Soc. Spec. Pub.* 42, 313–345.

Szopa K. 2009: The same reaction but different environment: breakdown of monazite in the High Tatra granites. *Mineralogia — Special Papers* 35, 113.

Szopa K., Gawęda A., Müller A. & Sikorska M. 2013: The petrogenesis of granitoid rocks unusually rich in apatite in the Western Tatra Mts. (S-Poland, Western Carpathians). *Mineral. Petrol.* 107, 609–627.

Thirwall M.F., Smith T.E., Graham A.M., Theodorou N., Hollings P., Davidson J.P. & Arculus R.J. 1994: High Field Strength Element Anomalies in Arc Lavas: Source or Process? *J. Petrol.* 35, 3, 819–838.

Uher P., Ondrejka M. & Konečný P. 2009: Magmatic and post-magmatic Y-REE-Th phosphate, silicate and Nb-Ta-REE-Y oxide minerals in A-type metagranite: an example from the Turčok massif, the Western Carpathians, Slovakia. *Miner. Mag.* 73, 6, 1009–1025.

Wark D.A. & Watson E.B. 2006: TitaniQ: a titanium-in-quartz geothermometer. *Contrib. Mineral. Petrol.* 152, 743–754.